Summer 2020

Multi-physics-based approach to active microwave thermography

Seyed Ali Mirala

Department: Electrical and Computer Engineering

Recommended Citation

Mirala, Seyed Ali, "Multi-physics-based approach to active microwave thermography" (2020). *Doctoral Dissertations*. 2917.
https://scholarsmine.mst.edu/doctoral_dissertations/2917

A MULTI-PHYSICS-BASED APPROACH TO ACTIVE MICROWAVE THERMOGRAPHY

by

SEYED ALI MIRALA

A DISSERTATION

Presented to the Faculty of the Graduate School of the

MISSOURI UNIVERSITY OF SCIENCE AND TECHNOLOGY

In Partial Fulfillment of the Requirements for the Degree

DOCTOR OF PHILOSOPHY

in

ELECTRICAL ENGINEERING

2020

Approved by:

Dr. Kristen M. Donnell, Advisor
Dr. Mohammad Tayeb Al Qaseer
Dr. Chulsoon Hwang
Dr. Garry Grubbs
Dr. Lesley Sneed

PUBLICATION DISSERTATION OPTION

This dissertation consists of the following three articles, formatted in the style used by the Missouri University of Science and Technology:

Paper I (pages 9-34): "Detection of Flat-Bottom Holes in Conductive Composites Using Active Microwave Thermography," published in ASME Journal of Nondestructive Evaluation, Diagnostics and Prognostics of Engineering Systems (JNDE).

Paper II (pages 35-64): "Active Microwave Thermography to Detect and Locate Water Ingress," accepted for publication in IEEE Transactions on Instrumentation & Measurement.

Paper III (pages 65-95): "Efficient Health Monitoring of RAM-Coated Structures by Active Microwave Thermography," to be submitted to IEEE Transactions on Instrumentation & Measurement.

ABSTRACT

The goal of this work is to advance a novel nondestructive testing (NDT) method for controlled, rapid, and effective inspection of a structure through the integration of microwave NDT and thermography, referred to as Active Microwave Thermography (AMT). In AMT, the structure under test is exposed to microwave radiation and the thermal profile of the structure is monitored via a thermal camera in order to obtain desired information regarding the structure. This new technique is applicable across a wide range of NDT needs including detection of voids, delamination, water ingress, debonding, and cracks in numerous structures such as carbon fiber and glass fiber reinforced polymers (CFRP and GFRP, respectively), cement-based materials, corroded metals, and structures coated with radio-frequency absorbing materials (RAM). This research is dedicated to three special cases among these applications of AMT; detection of voids in CFRP, evaluation of water ingress, and detection of delamination in RAM-coated structures. The effect of the structures' properties, excitation parameters, and defect size and location on the thermal response are investigated through analyses of technical outputs such as thermal contrast and signal-to-noise ratio. The main contributions of this research are first, enabling defect quantification through a formulation of the microwave heating and subsequently calculating the temperature's temporal and spatial variation. This formulation is validated through commercial simulation software and measurement. Second, it is shown (through simulation and measurement) that AMT is a reliable NDT technique that may be superior to other techniques for specific applications such as water ingress detection and inspection of RAM-coated structures.

ACKNOWLEDGMENTS

I am grateful with all of my being to my beloved wife, Mahshid Roshandelpir, for her dedication, enthusiasm, and love, and to my parents, for everything they gave me during my life. I believe I never could have embarked on my Ph.D. journey and finished it without an overwhelming support from them.

I would like to express my utmost gratitude to my advisor, Dr. Kristen M. Donnell, and Dr. Mohammad Tayeb Al Qaseer for their earnest support, inspirations, and the many hours they have devoted to me. It has been an extraordinary pleasure to work with them.

I am also grateful to Dr. Garry Grubbs and Dr. Lesley Sneed for their major contributions to this research and brilliant ideas, and to Dr. Chulsoon Hwang for serving on my committee and his valuable guidance.

This work was partially supported by the National Science Foundation Division of Electrical, Communication, and Cyber Systems (ECCS), Award No. 1609470, “A Multi-Physics-Based Approach to Active Microwave Thermography”.

TABLE OF CONTENTS

Page

SECTION

PAPER

SECTION

LIST OF ILLUSTRATIONS

PAPER I Page

PAPER II

PAPER III

LIST OF TABLES

PAPER I Page

PAPER II

PAPER III

SECTION

1. INTRODUCTION

1.1. ACTIVE MICROWAVE THERMOGRAPHY

Nondestructive testing and evaluation (NDT&E) of materials and structures plays an important role in aerospace and civil/infrastructure industries. In fact, many failures occur because of the presence of defects and imperfections in construction materials [1]. As such, many NDT&E techniques have been developed for structural health monitoring including visual inspection [2], microwave [3], ultrasound [4], X-ray [5], and thermography [6]-[8]. In thermography, the structure under test is exposed to a heat source that causes a temperature increase within the volume and over the surface of the structure. Typically, an active approach is used, meaning an active thermal source is utilized to induce thermal energy into the structure (as opposed to the passive approach in which the thermal source is natural, e.g., solar energy). The most commonly used thermal sources in active thermography are optical (i.e., flash lamp thermography, also often referred to as conventional thermography) [6], ultrasonic [9], eddy current [10], and more recently, microwave [11].

Active microwave thermography, or AMT, is a relatively new active thermographic method that has demonstrated potential in recent years for many NDY&E applications including health monitoring of carbon fiber reinforced polymer (CFRP) structures [12],[13], assessment of microwave absorbing structures [14], detection and evaluation of surface cracks in metal structures [15], characterization of corroded reinforcing steel bars

[16], evaluation of steel fiber distribution in cement-based mortars [17], defect detection of CFRP-strengthened cement-based materials [18],[19], and mines detection [20].

In AMT, the structure under test is exposed to microwave radiation. Depending on the electromagnetic properties of the structure's constitutive materials, two heating mechanisms may occur that are referred to as dielectric heating and Joule heating [21],[22]. Dielectric heating results from absorption of microwave energy in lossy dielectric materials. Generally, dielectric materials are described by their (relative to freespace) complex dielectric properties as $\varepsilon_r = \varepsilon_r' - j\varepsilon_r''$, where ε_r' (relative permittivity) represents the ability of a dielectric material to store microwave energy, and ε_r'' (relative loss factor) represents the ability of a material to absorb energy. Thus, when a lossy material is irradiated with microwave energy, dielectric heating occurs as a result of the absorbed energy. Joule heating, on the other hand, occurs due to current induced on the surface of conductive materials. More specifically, when a microwave signal impinges on a conductive material, surface current is induced on the conductor surface due to the electric conductivity (σ) of the material, which in turn results in ohmic losses. In addition, this induced surface current can serve as a source of radiated (or scattered) microwave energy, which in turn may be absorbed by nearby dielectric materials.

Subsequent to the microwave-induced heating, the thermal energy (heat) diffuses inside the structure and causes a temperature increase within the volume and over the surface of the structure. The existence of any inconsistency in the structure (such as a defect) affects the heat diffusion and in turn affects the surface temperature distribution which is monitored via a thermal camera. Thermal images captured over time by the thermal camera may provide information regarding potential defects in the structure. Void-type defects such as holes and open cracks act as thermal insulators that impede against further diffusion of the heat to the deeper parts of the structure and lead to a high concentration of thermal energy. This manifests as a hot spot on the structure surface and is evident in the thermal measurements. Therefore, the temperature increase can be used as a metric to evaluate the defects. In another case, the defect may act as a source of thermal energy when it is exposed to the microwave radiation. For example, water ingress or moisture within a (lower loss) dielectric structure can absorb microwave energy, resulting in generation of heat and a subsequent thermal contrast that can be monitored via the thermal camera.

In general, AMT has several advantages including short inspection times for relatively large areas, non-contact interrogation and inspection, and easy-to-interpret results (results are obtained in an image format and can be visually interpreted to some extent). Beside these advantages that AMT shares with other thermographic methods [23], microwave radiation as the thermal excitation can be superior to other excitations (e.g., optical, in conventional thermography) in special cases, as is discussed in the following section.

1.2. RESEARCH OBJECTIVE

The goal of this dissertation is to provide a comprehensive quantitative analysis tool that relates AMT outputs to potential defect features as well as to introduce new applications for this technique.

When the application of AMT in several cases, such as defect detection of CFRP-strengthened cement-based materials, is already established (as a proof-of-concept), there often remains a lack of quantitative and comparative analysis for the particular inspection. This research aims to fill this gap by proposing a physical model and pertinent mathematical formulation. This is accomplished for three distinct applications. In the first case, detection of void-type defects, standardized as flat-bottom holes (FBH), in conductive composites, in particular CFRP, is quantitatively studied. In this case, since conductive materials (such as CFRP) do not allow penetration of electromagnetic energy, the microwave excitation solely generates a surface thermal source through induced surface current (as mentioned above). In this way, this thermal generation is similar to conventional thermography where the optical impulse is only absorbed at the surface of the sample. After calculating the surface thermal source from induced surface currents and the Joule heating principle, the heat equation, which relates the temperature distribution to the thermal sources, is solved numerically using a finite difference approach. Specifically, to include the effect of an FBH on the temperature, an adiabatic boundary condition is applied over the boundaries of FBH, meaning that there is no heat flux through the boundary. As an FBH impedes the diffusion of thermal energy further into the deeper parts of the sample, a higher temperature will be observed over the FBH on the sample surface. To quantify this effect, the thermal contrast is defined as the difference between the temperature increase of a defective area and that of a sound/healthy area. For a successful detection of an FBH, the thermal contrast must exceed the thermal camera's sensitivity. Based on this, detection likelihood is quantified through calculation of thermal contrast caused by an FBH and its diameter and depth. In other words, a dimensional analysis of detectable FBHs is provided including a radius-to-depth ratio threshold for successful detection. The mathematical formulation discussed above (and formulated here for the first time) also enables investigation of the effect of microwave excitation power and frequency on the AMT results. This mathematical analysis is validated via comparison with a coupled full wave electromagnetic/thermal model developed using CST Microwave Studio® (CST MWS) and CST MultiPhysics Studio® (CST MPS), as well as through several measurements.

Another objective for this research arises from the fact that use of a microwave excitation is particularly well-suited for detection of water ingress due to the fact that water is highly absorptive to electromagnetic energy in the microwave frequency range. Evaluation of water ingress and moisture content in composited (mainly GFRP and honeycomb structures) is very important to ensure that mechanical properties of composites are negatively unaffected. For this application, AMT offers the advantage of selective heating as the thermal excitation is applied solely to the water ingress, with reduced interaction with the background material. In other words, unlike conventional thermography, the defect (water) acts as a heat source, rather than merely affecting the heat diffusion. To formulate this case, the interaction of the incident microwave energy and the water volume (a dielectric) is considered. More specifically, the electromagnetic loss (and hence the generated heat) inside the water ingress is calculated. Knowing the heat source as such, the temperature is calculated via the Green's function method [24]. Using the Green's function method as an analytical approach is computationally more efficient (i.e., is faster and requires reduced memory resources) than numerical techniques and commercial simulation software packages. The selective heating of water ingress and the need for detection of water ingress in structures including aviation, submarine acoustic tiles, heavy electrical component insulators, etc. show the importance of AMT for this application, as discussed in this dissertation.

As the third case studied in this dissertation, the use of AMT for detection of delamination in RAM-coated structures (extensively used in aerospace and military applications) is quantitatively studied for the first time. AMT is an especially good candidate for inspection of such structures due to the inherent electromagnetic properties of the RAM itself. In other words, these materials are designed to reduce (through energy absorption) the amount of electromagnetic energy that is scattered (or reflected) from (subsurface) conductive materials. Thus, from an AMT perspective, the RAM, when under microwave illumination, absorbs the energy and subsequently undergoes a temperature increase; an essential component in thermographic techniques. In addition, unlike conventional thermography in which heat is generated mostly at the surface, the microwave heating takes place throughout the RAM volume (as well as its surface). In this way, the thermal source is located flush against the substructure rather than at the surface of the coating and hence the detection capability may be improved. In these cases, AMT is uniquely effective and potentially superior to other thermographic methods and as such, this dissertation is dedicated to such applications.

1.3. ORGANIZATION OF THE DISSERTATION

This dissertation focuses on three distinct applications of AMT as are summarized below.

PAPER I, titled “Detection of Flat-Bottom Holes in Conductive Composites Using Active Microwave Thermography” investigates the potential of AMT for detection of flat-bottom holes (FBHs) in conductive composites such as carbon fiber-based composites. To this end, a formulation is first established as mentioned in the previous section. Then, the simulation (using CST MWS and MPS) and experimental results are presented that validate the formulation and show the AMT outcomes in potential situations where a carbon fiber reinforced polymer (CFRP) laminate contains FBHs. These results illustrate the potential for AMT as a nondestructive testing (NDT) tool for inspection of CFRP structures. More specifically, the effect of FBH radius and depth (or combined as the radius-to-depth ratio) on the detection likelihood is studied. By considering the thermal contrast, it is shown that detection likelihood can be improved by increasing the microwave frequency or power level. Furthermore, AMT measurements are presented for a number of FBHs machined in a multidirectional CFRP sheet, and the signal-to-noise ratio (SNR) in thermal images over time is monitored that shows a high level of defect information relative to background noise (>20 dB) is achievable after about 60 sec of microwave excitation.

PAPER II, titled “Active Microwave Thermography to Detect and Locate Water Ingress,” reports on the application of AMT to detect and locate water ingress within a structure. This paper presents a mathematical formulation (as discussed previously) along with simulation and measurement results. The mathematical formulation relates the water volumetric distribution and location to the temperature distribution over the inspection surface. Moreover, a method for evaluating the depth of water ingress is developed which is based on the delayed time when the maximum of temperature rise occurs. This formulation is considered for three water ingress cross-sectional distributions named as point (like drops), linear (such as water seeped into a crack or vein), and extended. Following the analysis, AMT measurement results of a small volume of water, placed in a rubber sample at predetermined locations, are presented. Analysis of the measurement data indicates the potential of AMT for not only detection of water ingress, but also accurate depth estimation of small amounts of water ingress. Specifically, 0.5 mL of water (equivalent to 10 drops) is clearly detected (experimentally) after 120 seconds of microwave excitation, in a rubber sample. More importantly, the depth of water is estimated using experimental data and a mathematical formulation, with an average quantification error of ~5%. In addition, the relationship between the detectability of water and test parameters including the microwave excitation frequency and power, water volume and depth, structure constitutive properties, and the heating time is studied.

In PAPER III, titled “Efficient Health Monitoring of RAM-Coated Structures by Active Microwave Thermography,” results of a comprehensive study on the application of AMT for health monitoring of structures coated with radio-frequency absorbing materials (RAM) is presented. It is shown that AMT is unique for this particular application since the microwave excitation acts as a highly efficient thermal source due to the inherent absorptive electromagnetic properties of RAM-coated structures. In addition, the microwave-induced heating takes place within the volume of a RAM-coated structure (as the microwave energy propagates through the RAM), as opposed to solely heating the surface (as is the case in conventional thermography). Specifically, this work focuses on detection of delamination, which is a common defect in CFRP structures, via AMT. To this end, as mentioned earlier, a mathematical model is developed that relates the thermal contrast to the delamination, microwave excitation, and the structure properties. Subsequently, measurements are conducted showing that delaminations with a diameter as small as 1 cm concealed under a 2-mm thick layer of RAM can be reliably detected by applying 1 minute of microwave excitation.

PAPER

I. DETECTION OF FLAT-BOTTOM HOLES IN CONDUCTIVE COMPOSITES USING ACTIVE MICROWAVE THERMOGRAPHY

ABSTRACT

Active Microwave Thermography (AMT) is an integrated nondestructive testing (NDT) technique that utilizes a microwave-based thermal excitation and subsequent thermal measurement. AMT has shown potential for applications in the transportation, infrastructure, and aerospace industries. This paper investigates the potential of AMT for detection of defects referred to as flat-bottom holes (FBHs) in composites with high electrical conductivity such as carbon fiber-based composites. Specifically, FBHs of different dimensions machined in a carbon fiber reinforced polymer (CFRP) composite sheet are considered. Simulation and measurement results illustrate the potential for AMT as a nondestructive testing (NDT) tool for inspection of CFRP structures. In addition, a dimensional analysis of detectable defects is provided including a radius-to-depth ratio threshold for successful detection.

1. INTRODUCTION

Nondestructive testing (NDT) of infrastructure is important to many industries including aeronautics and transportation as it relates to the inspection of carbon fiber reinforced polymer (CFRP) structures. Several NDT methods including microwave, ultrasound, x-ray, and thermography (active and passive) have been applied to the aeronautical and transportation industries (with varying levels of success) for inspection of infrastructure and composites [1]-[7]. Among these methods, microwave NDT is very limited for inspection of subsurface defects in conductive materials due to the lack of penetration of microwave energy into such materials. Additionally, while surface inspections of conductive materials are feasible, often the inspection time may be significant due to the need for raster scanning of the area of interest. Acoustic methods are successful in many arenas and are well-established. However, they often require operator expertise and contact with the material/structure under test. X-ray or computed tomography is also quite promising for many applications, but brings significant safety requirements and precautions [4]. Thermography, both active and passive, is another well-established and successful technique. Passive thermography utilizes natural sources of thermal energy such as solar energy, structural loading, moisture evaporation, air movement, etc. On the other hand, active thermography utilizes an active source of thermal energy such as a flash lamp (as is used in traditional thermography), quartz lamp, electromagnetic, acoustic, etc. Passive thermography implies no control of the applied energy; rather, simply observing with an infrared camera, whereas active thermography implies control of the applied energy (for the purpose of inspection). Active thermography has been successfully applied to a number of NDT needs including defect detection in composite materials [5]-[7].

Active microwave thermography (AMT) is a relatively new NDT technique that is based on the integration of microwave and thermographic NDT [8]-[15]. In AMT, microwave energy is utilized to heat a structure of interest, and the resulting surface thermal profile is monitored via a thermal camera. Compared to traditional (flash lamp) thermography, AMT does not require substantial amounts of power [12], and several (electromagnetic) parameters can be optimized in order to tailor the inspection to a specific material including frequency and polarization. Recently, AMT has been utilized for detection of corrosion on steel [11], evaluation of steel-fiber reinforced concrete [12], and inspection of structures strengthened with unidirectional CFRP [13]-[15], with promising results.

In general, when using a microwave-based thermal excitation, there are two possible heating mechanisms that may take place; dielectric heating and Joule heating. Dielectric heating takes place when the structure under test contains (lossy) dielectric materials. In general, the ability of a dielectric to generate heat is determined by its loss factor (ε'') which appears as the imaginary part of its complex dielectric constant ($\varepsilon = \varepsilon' - j\varepsilon''$). Due to the lossy electromagnetic properties of the material, microwave energy is absorbed and converted into heat. The real part of dielectric constant, on the other hand, represents the ability of the material to store electromagnetic energy. The other heating mechanism, Joule heating, occurs when conductive materials are present in the structure. When a conductor is exposed to electromagnetic radiation, depending on its electrical conductivity (σ), currents are induced on the surface of the conductive material. These currents serve as a secondary thermal excitation, as ohmic losses (which cause a subsequent thermal increase) occur when currents flow in a conductive material. In addition to direct ohmic losses, these induced currents may also serve as a secondary source of (reradiated) electromagnetic energy which can be subsequently absorbed by other nearby lossy dielectrics (such as the epoxy in CFRP materials).

In all cases, the heat generated from the electromagnetic energy diffuses throughout the material. Since defects and discontinuities affect the heat diffusion, a temperature difference on the surface of the structure will result if a defect is present. Analyzing the surface temperature profiles captured during an AMT inspection allows the defects to not only be detected, but also characterized. As such, this paper investigates a new application of AMT as an NDT tool for inspecting defects in conductive (specifically CFRP) composites. The defects are modeled as cylindrical holes that are referred to as flat-bottom holes (FBHs) [16]. Representative simulated and measurement results are provided, showing the applicability of AMT for such inspections.

2. SIMULATION AND ANALYSIS

In order to investigate the utility of AMT for inspection of FBHs in conductive materials, numerical modeling was conducted. More specifically, a finite slab containing an FBH under plane wave excitation is considered, as is illustrated in Figure 1. The height of the dielectric slab is denoted as h, and the radius and depth of the defect are given as r and d, respectively.

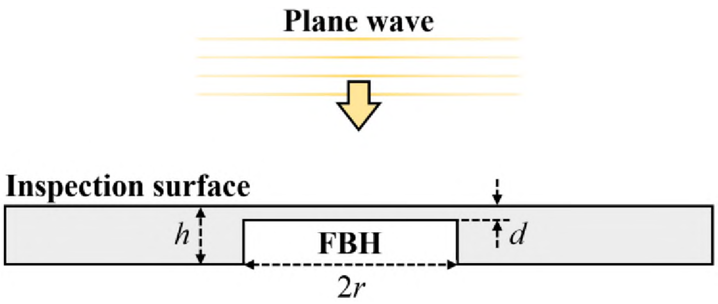

Figure 1. Geometry of the simulated model

Upon contact with the structure under inspection, portions of the incident plane wave will be reflected, absorbed by, and transmitted through the material. The absorbed energy is converted to heat and therefore can be considered as a thermal source. For a highly conductive material, there will be not be any energy transmitted through the material. Thus, the incident energy is either reflected or absorbed. Further, for highly conductive materials, most of the incident energy will be reflected. The energy that is not reflected is absorbed within a very thin layer (essentially the surface) of the material. This layer is dimensionally on the order of the material's skin depth, δ, which is defined as $\delta = \sqrt{1/\pi f \mu \sigma}$, where f and μ are the incident wave frequency and material permeability, respectively. A CFRP laminate with electrical conductivity of σ = 50,000 S/m, for example, has a skin depth of ~46 μm at f = 2.4 GHz. As such, the thermal source can be considered as a uniform (due to the plane wave excitation) surface heat source, *Qs*, on the surface of the structure. Specifically, *Qs* may be quantified as:

$$Q_s = P_{inc} - P_{ref} = P_{inc}(1 - |\Gamma|^2) \quad (1)$$

where Pinc and Pref are the incident and reflected wave power densities and Γ denotes the electromagnetic wave reflection coefficient of the air-structure interface and is defined at $\Gamma = (\eta - \eta_0)/(\eta + \eta_0)$. In this formula, η is the characteristic impedance (ratio of electric to magnetic fields of any electromagnetic wave in the medium) of the conductive material and is given by $\eta \cong \sqrt{\omega\mu/\sigma}$, and η_0 is the characteristic impedance of freespace (i.e., 120π) [17].

The heat source of Eq. (1) generates thermal energy which extends throughout the structure volume over time. To calculate the time-dependent temperature distribution, T, the source-free heat equation given in Eq. (2) should be solved. The volumetric heat source in Eq. (2) is considered to be zero since there is no heat source inside the structure and the surface heat source over the inspection surface will be applied as an inflow heat flux boundary condition.

$$\rho c_p \frac{\partial T}{\partial t} = \nabla \cdot (\mathbf{k} \cdot \nabla T) \tag{2}$$

Here ρ, c_p, and $\mathbf{k}$ are the density, specific heat, and thermal conductivity tensor, respectively. The thermal conductivity, $\mathbf{k}$, is considered a tensor due to the potential anisotropy of the structure. For example and as it relates to this work, the thermal conductivity for a CFRP laminate differs for the in-plane and along-the-depth (or transverse) directions (i.e., parallel and perpendicular to its embodied fibers, respectively). However, the same thermal conductivity is assumed along any in-plane direction. This assumption is valid for multidirectional fiber-reinforced composites as their fibers are oriented in several in-plane directions, rendering the same electrical and thermal behavior along these directions. Unidirectional composites, on the other hand, have different behaviors along the two in-plane normal directions of parallel- and perpendicular-to-the-fibers, requiring assignment of different values to the electrical and thermal conductivities in these directions. Taking this into consideration and assuming a cylindrical coordinate system with the z-axis being the axis of the FBH (modeled as a cylinder), the in-plane isotropy of thermal conductivity leads to angular symmetry of temperature (i.e. $\partial T/\partial \varphi = 0$). As such, Eq. (2) can be expressed in cylindrical coordinates as [18]

$$\rho c_p \frac{\partial T}{\partial t} = \frac{1}{r}\frac{\partial}{\partial r}\left(r k_r \frac{\partial T}{\partial r}\right) + \frac{\partial}{\partial z}\left(k_z \frac{\partial T}{\partial z}\right) \tag{3}$$

where T is a function of space and time, and material properties ρ, c_p, k_r, and k_z are a function of space (due to the inhomogeneity of CFRP and air). The values used in simulation for these parameters are provided in Table 1 [19], [20].

Table 1. Material properties

Material	**Property**	**Value**
CFRP	Electrical conductivity	σ = 50,000 S/m
	In-plane thermal conductivity	k_r = 2 W/m·K
	Transverse thermal conductivity	k_z = 0.5 W/m·K
	Density	ρ = 1500 kg/m^3
	Specific heat capacity	c_p = 800 J/kg·K
Air	Thermal conductivity	k = 0.026 W/m·K
	Density	ρ = 1.204 kg/m^3
	Specific heat capacity	c_p = 1005 J/kg·K

Discretizing space and time as $r = i\Delta r$, $z = j\Delta z$, and $t = k\Delta t$, where i, j, and k are discretized coordinates, and Δr, Δz, and Δt are space and time steps, and using a forward-time centered-space (FTCS) scheme, finite difference approximations to each term in Eq. (3) may be written as:

$$\rho c_p \frac{\partial T}{\partial t} \simeq \rho(i,j) c_p(i,j) \frac{T^{k+1}(i,j) - T^k(i,j)}{\Delta t} \tag{4}$$

$$\begin{aligned} \frac{1}{r}\frac{\partial}{\partial r}\left(r k_r \frac{\partial T}{\partial r}\right) \simeq \frac{1}{i\Delta r} \\ \times \frac{1}{\Delta r}\left\{[(i+1/2)\Delta r] k_r(i+1/2\,,j) \frac{T^k(i+1,j) - T^k(i,j)}{\Delta r}\right. \\ \left. - [(i-1/2)\Delta r] k_r(i-1/2\,,j) \frac{T^k(i,j) - T^k(i-1,j)}{\Delta r}\right\} \end{aligned} \tag{5}$$

$$\begin{aligned} \frac{\partial}{\partial z}\left(k_z \frac{\partial T}{\partial z}\right) \simeq \frac{1}{\Delta z}\left\{k_z(i,j+1/2) \frac{T^k(i,j+1) - T^k(i,j)}{\Delta z}\right. \\ \left. - k_z(i,j-1/2) \frac{T^k(i,j) - T^k(i,j-1)}{\Delta z}\right\} \end{aligned} \tag{6}$$

Also, boundary conditions are incorporated as:

$$\begin{cases} k_n \dfrac{\partial T}{\partial n} = Q_s - h_c(T - T_a) & top\ surface \\ \dfrac{\partial T}{\partial n} = 0 & all\ other\ surfaces \end{cases} \tag{7}$$

where n, h_c, and T_a denote the direction normal to the boundary, convective heat transfer coefficient, and ambient temperature, respectively. The top surface boundary condition of Eq. (7) represents the heat generated by the microwave excitation and thermal energy loss due to convection. The remaining surfaces utilize the adiabatic boundary condition, meaning that the heat flux from these boundaries is assumed zero. A stable solution of Eqs. (4)-(6) satisfies the stability condition [21] given as

$$\Delta t \leq \frac{1}{2\alpha_{max}(1/\Delta r^2 + 1/\Delta z^2)} \tag{8}$$

where α_{max} denotes the maximum thermal diffusivity of the materials involved.

The numerical model given above provides the temporal evolution of temperature in the material/structure. The temperature is subsequently analyzed over the inspection surface of the structure to predict the thermal profiles captured in practice by a thermal camera during an AMT inspection. Using this numerical technique is advantageous over commercial electromagnetic/thermal simulation software packages since it utilizes an analytical electromagnetic solution given in Eq. (1), instead of a time-consuming full-wave numerical solution. Specifically, due to the small skin depth (micrometers or less) of conductive materials, the mesh size should be taken comparably small and subsequently require a huge memory resource and processing time. Furthermore, the spatial two-dimensional heat transfer equation given in Eq. (3) (which has two spatial coordinates, *r* and *z*) is used rather than a three-dimensional simulation. Therefore, the simulations may run remarkably faster while providing accurate results (as will be shown later). The simulation time becomes specifically important when evaluating defects by a reverse approach. In such cases, the simulation is iteratively solved with swept values for dimensions in order to find the best match between the simulation and measurement results.

To quantify the temperature variation over the structure's inspection surface (in order to evaluate potential defects), the temporal temperature increase, $\Delta T(x,y,t)$ is defined as

$$\Delta T(x,y,t) = T(x,y,t) - T(x,y,0) \quad (9)$$

where $T(x,y,t)$ is the temperature distribution on the surface under inspection at a given time t, and $T(x,y,t)$ is the initial temperature distribution. Using ΔT instead of the absolute temperature, T, eliminates the effect of the initial temperature distribution over the surface and represents the temperature change resulting only from the microwave excitation. Another important parameter, referred to as the thermal contrast, (TC), is defined (temporally) as:

$$TC(t) = \langle \Delta T(x,y,t) \rangle_D - \langle \Delta T(x,y,t) \rangle_S \quad (10)$$

where $\langle \cdot \rangle_S$ and $\langle \cdot \rangle_D$ denote the average over a given sound and defective area, respectively. Defective and sound areas refer to areas on the inspection surface above the location of defective and sound areas within the structure (as most defects are located beneath the surface). Therefore, the TC, as defined in Eq. (10), represents the temperature difference caused by the defect and can be used to evaluate the defect.

For an air-filled defect such as an FBH, a positive TC is expected as the air is a good thermal insulator and therefore reduces the loss of thermal energy through diffusion.

As it relates to heat diffusion, FBHs with larger cross-sections and smaller depths will result in less radial and transverse heat diffusion, as compared to smaller or deeper FBHs. Therefore, the TC is expected to increase with FBH radius and decrease with depth. To verify these expectations and further study the detectability of FBHs as a function of dimensions, the TC obtained using the numerical technique discussed above and a coupled electromagnetic/thermal model created in CST MPHYSICS STUDIO (CST MPS) are shown as a function of depth for FBHs with 10, 15, and 20 mm radii in Figure 2. The structure's height (*h*) is assumed to be 5 mm and the microwave excitation is applied for 420 sec. Also, the frequency and power level of the incident energy are 2.4 GHz and 50 W (respectively) in all simulations (to be consistent with the measurement results given in Measurement Results Section).

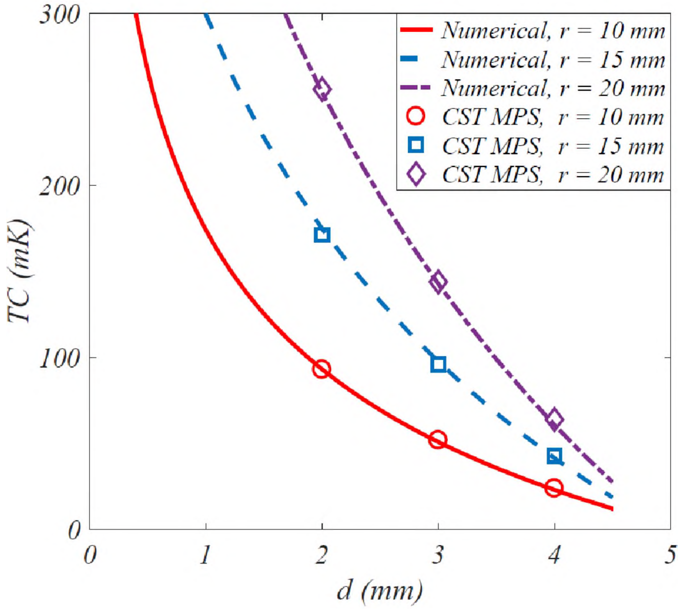

Figure 2. Thermal contrast versus FBH depth for different radii obtained through numerical analysis and CST MPS simulations

The results of Figure 2 show good agreement between those of the above-mentioned numerical model and those obtained via CST MPS. As a result, the numerical approach developed for this work is used for all simulations hereafter. As is also evident in Figure 2, the TC is dependent on the depth and radius of the FBHs. This quantity can be used to estimate the detection likelihood of a FBH with a certain *r* and *d*. To this end, TC is provided as isothermal contours versus r and d in Figure 3. From this, it's noticeable that the TC decreases from the top-left corner of the *r*-*d* plane, which represents high *r*/*d* ratios, to the right-bottom corner, where *r*/*d* ratios are small. This ratio, called aspect ratio, is often used to estimate the detectability of a defect in traditional thermography [16]. Similarly, this ratio can be used as an estimate of defect detectability in AMT.

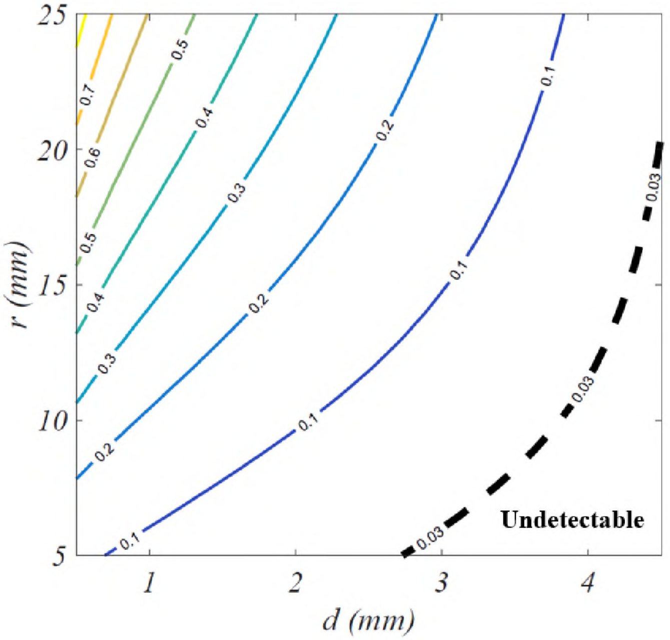

Figure 3. Thermal contrast isothermal contours for different radii and depths of FBHs

Theoretically, the minimum TC required for a successful detection is equal to the sensitivity of thermal camera used for measurement. As such, for any given structure, microwave excitation, and thermal camera, a region in *r-d* plane exists which yields any combination of r and d for which FBHs are likely not detectable. In Figure 3, this undetectable region occurs when TC falls below 30 mK, the sensitivity of the thermal camera used for measurements. However, in order to improve detection of such defects, the power level or frequency of the microwave excitation can be increased in order to increase the TC or using a thermal camera with lower sensitivity. In fact, according to Eq. (1), the surface heat source (Q_s) is linearly proportional to the incident power (P_{inc}). Also, the intrinsic impedance of a conductor increases with frequency ($\sqrt{\omega\mu/\sigma}$) and becomes more similar to that of freespace, thereby reducing the amount of reflected energy and increasing the absorbed energy. Therefore, as the TC is proportional to the absorbed power, it would will also increase with increased excitation power and frequency. To verify this, Figure 4 shows the TC after applying 420 sec of microwave excitation as a function of frequency (in the operational band of the AMT system used for measurements) and excitation power for an FBH with $r = 8$ and $d = 4$ mm (an undetectable FBH per Figure 3). According to Figure 4, the TC meets the measurement threshold for a 75 W microwave excitation operating at a frequency greater than 3 GHz, or with a 100 W excitation and a frequency greater than 1.7 GHz. Therefore, for detection of any given FBH and temperature measurement sensitivity, there is a combination of minimum excitation power and frequency that must be met. However, practically speaking, this threshold may not be achievable, as increasing the power level and frequency both increase system cost. In addition, safety risks may also result as the power is increased. More specifically, for normal environmental conditions and for incident electromagnetic energy of frequencies from 10 MHz to 100 GHz, the radiation protection guide regulated by the Occupational Safety and Health Administration (OSHA) is 10 mW/cm^2 as averaged over any possible 0.1-hour period [22]. In this work, compliance with the OSHA radiation standard is achieved at least ~80 cm from the horn antenna aperture. As it relates to the safety of the operator, if the operator remains outside of this area, OSHA compliance is achieved. Furthermore, utilization of specific frequencies may be restricted by the United States' Federal Communications Commission (FCC), or similar regulatory bodies in other countries. To comply with FCC regulations, the operating frequency of 2.4 GHz is used, which is in the unlicensed frequency band allocated for industrial, scientific and medical (ISM) applications.

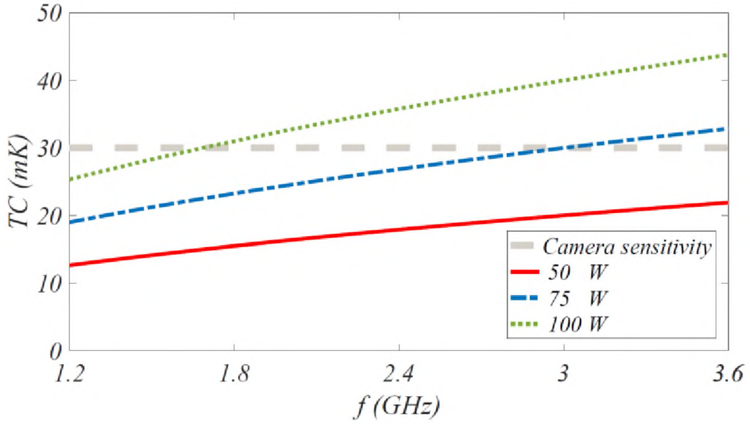

Figure 4. Thermal contrast as a function of frequency for different microwave excitation powers

3. MEASUREMENT RESULTS

In order to further illustrate the potential for AMT to inspect CFRP structures, representative measurements on a CFRP sample, shown in Figure 5, were made. The sample has a thickness (*h*) of 5 mm, and includes nine FBHs with radii of 10, 15, and 20 mm, each with depths of 2, 3, and 4 mm. The other side of the sample is intact and is the interrogation and viewing side (i.e., surface that is excited by microwave energy and subsequently viewed with the thermal camera). The CFRP sample consists of a number of thin carbon fiber layers placed at various angles with respect to each other. Thus, the overall sample consists of fibers that can be assumed to be located at all angles (from 0 deg to 180 deg). As such, the thermal and electrical properties of the sample are identical along any in-plane direction (as discussed above for CFRP of this type). However, the fibers are transverse to the sheet normal direction which causes the along-the-depth properties differ from those of the in-plane.

Figure 5. Photograph of the CFRP sample with 9 (machined) FBHs with different radii and depths

The measurement setup is shown in Figure 6 and consists of a microwave source and amplifier, horn antenna, thermal camera, and control and data acquisition (DAQ) unit. The thermal camera used in this work is the FLIR T430sc, with the specifications shown in Table 2. The control and DAQ units synchronize the microwave and thermal segments of the AMT system. All measurements are conducted at a frequency of 2.4 GHz and power level of 50 W. The horn antenna faces directly toward the sample surface to maximize the microwave-induced heat over the surface. The sample was placed a distance of 17 cm from the antenna's aperture (herein referred to as the lift-off distance). This distance was chosen to ensure that the microwave excitation was sufficiently uniform over the inspection area but also allowed viewing of the sample surface with the thermal camera. More specifically, as a result of the electric field distribution of the horn antenna at the location of the sample, the energy is mostly focused over an area commensurate with the aperture size (23×17 cm^2). The camera has a skewed view of the sample surface. The measurement setup is fixed during the entire measurement process. The thermal profiles taken by the thermal camera are subsequently rotated by post-processing in order to remove the effect of the skew angle. The sample is placed on a thermal insulator (Styrofoam) to avoid thermal losses from the bottom surface.

Table 2. Thermal camera specifications

Parameter	**Value**
Detector type	Uncooled microbolomer
Wavelength band	7.5 – 13.0 μm
Detector size	320 × 240
Temperature resolution (NETD)	< 30 mK
Temperature range	-20^{o}C - 120^{o}C
Optics	Integrated lens 18 mm (25^o)
Frame rate	30 Hz

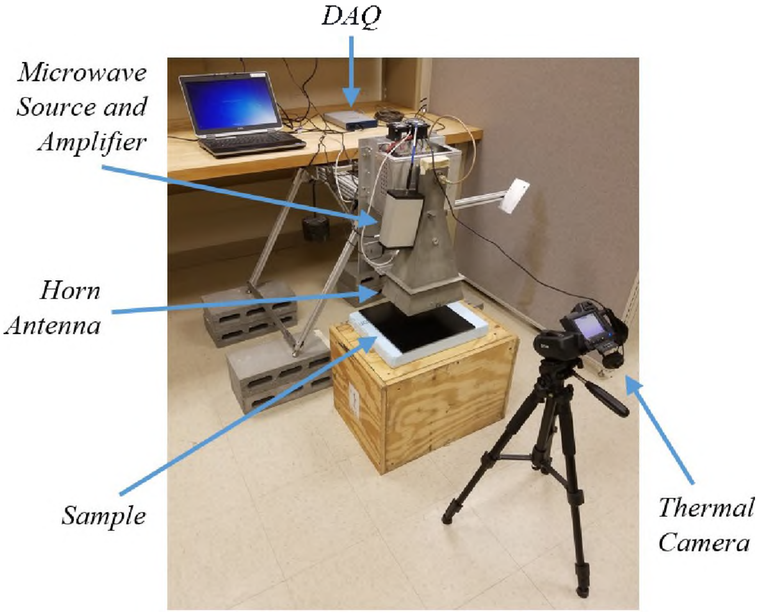

Figure 6. Active microwave thermography measurement setup

The measurements were conducted for a total excitation time of 420 sec (as in simulations). In order to observe the effect of defects on the thermal profile over the sample surface, Figure 7 illustrates the surface thermal profile for an FBH with $r = 20$ mm and $d = 2$ mm at three instances of time within the excitation period.

The temperature increase is evident in both the defective and sound areas in Figure 7. However, the temperature increases more rapidly over the defective area (the middle point of each image), resulting in a finite TC and a detectable FBH. This is significant in that while microwaves do not interact with the FBH directly, the FBH can still be detected due the effect of the FBH on thermal diffusion. This property of AMT is unique among microwave-based inspections, as traditional microwave NDT relies on the direct interaction of microwaves and materials, therefore finding application for subsurface defect detection in dielectric materials, but only surface inspections of conductive materials (such as CFRP). The variations in the background are partly due the proximity of other FBHs and the sample edges to the main FBH under inspection. Furthermore, noise from environment (e.g., thermal energy from undesired sources reflected by the sample and captured by thermal camera), emissivity variations over the inspection surface, thermal camera noise, etc. show up in the thermal profiles. As the temperature values are small, the temperature variations are significant and easily seen.

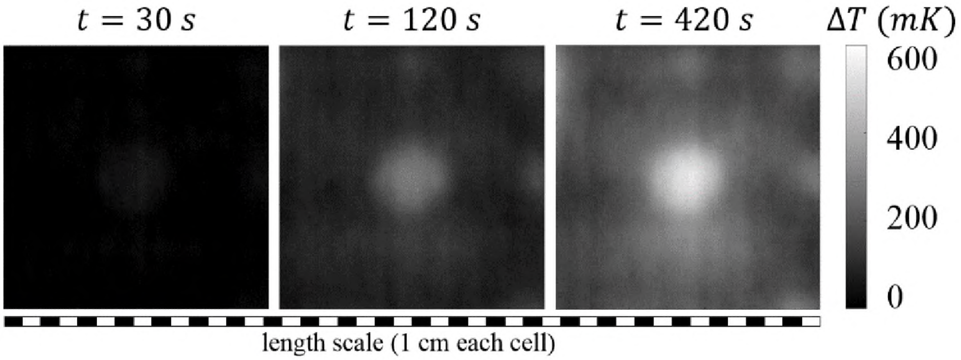

Figure 7. Thermal profile images for FBH with $r = 20$ mm and $d = 2$ mm captured at different instants of time

To illustrate the effect of FBH radius and depth on the TC, measurement results for three FBHs with a 20 mm radius and depths of 2, 3, and 4 mm are shown in Figure 8(a), and measurement results of three additional FBHs with a depth of 2 mm and radii of 20, 15, and 10 mm are shown in Figure 8(b). Each measurement is repeated three times and the results are averaged. The TC is calculated based on the average measured temperature over 100 pixels for both defective and sound areas, in addition to a temporal average that is calculated over 100 frames. These averaging processes highly suppress temperature fluctuations due to noise. As seen in Figure 8(a), the TC increases at a slower rate for deeper FBHs. In addition, the asymptotic maximum TC is also inversely proportional to depth. Similarly, as is evident in Figure 8(b), the rate of increase of the TC is also proportional to FBH radius (i.e., larger radius, larger rate of increase). Both of these behaviors are as expected, per the results of simulations. Specifically, the TC at $t = 420$ sec for the curves of Figure 8(a) are roughly 260, 160, and 110 mK and they are 260, 150, and 90 mK for the curves given in Figure 8(b). These values are in good accordance with the corresponding simulated TC values given in Figure 2 for the simulated FBHs with the same radius and depth. This validates the presented simulation model as well as illustrates the potential of AMT for detection of FBHs in electromagnetically conductive structures.

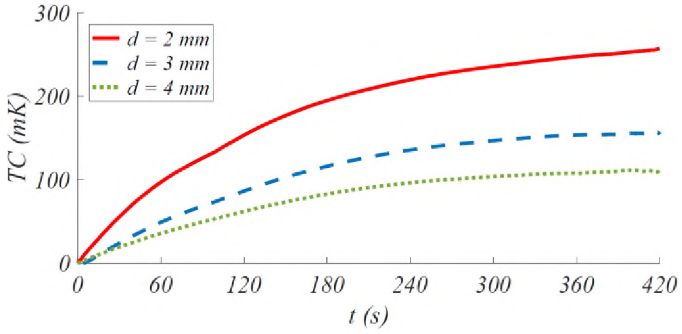

(a)

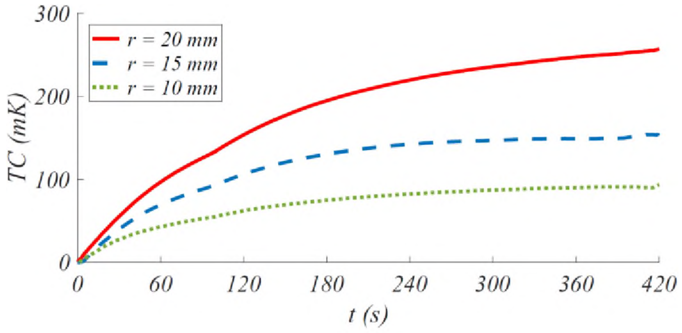

(b)

Figure 8. Thermal contrast as a function of time for FBHs of (a) $r = 20$ mm and different depths and (b) $d = 2$ mm and different radii

To investigate the effect of sample distance and orientation with respect to the antenna on the AMT inspection results, Figure 9 illustrates the TC versus time for an FBH of r = 20 mm and d = 2 mm for two different lift-offs and two orthogonal polarizations (referred to as P1 and P2). The polarization refers to the orientation of the incident electric field. Since the antenna is linearly polarized, the sample was rotated 90° with respect to the antenna to see the effect of polarization. As is evident in Figure 9, a smaller lift-off results in a larger TC due to the increase in incident power level impinging on the sample surface (i.e., reduced free-space losses). In addition, for a given lift-off, the TC is independent of polarization. This is due the multidirectional nature of the fibers within the CFRP sample (discussed above), causing the same electrical and thermal properties for all in-plane directions. Hence, selection of the polarization of the microwave excitation is not a concern for this sample. However, if the fibers are oriented in a single direction (i.e. unidirectional CFRP), the optimum electric field polarization is perpendicular to the fiber orientation so that the incident energy can penetrate into the sample and generate more heat, thereby providing a better TC (as is shown in Ref. [13]).

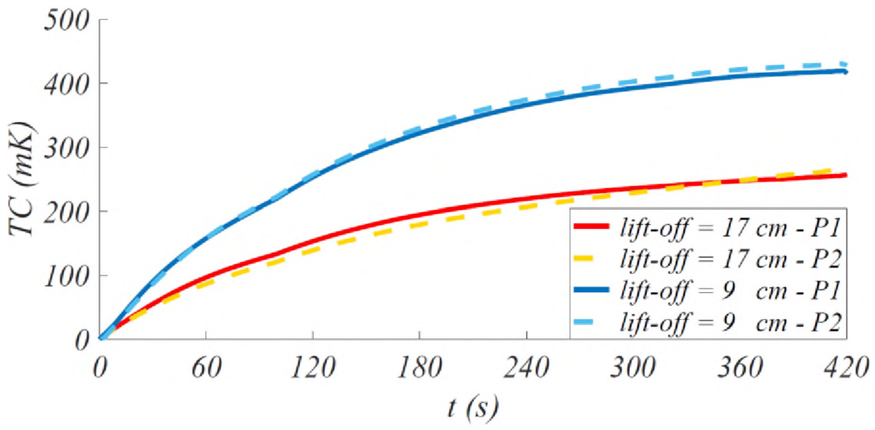

Figure 9. Thermal contrast for different lift-offs and polarizations

In AMT inspections, the temperature distribution is subject to non-ideal temporal and spatial variations due to noise from the environment, emissivity variations over the inspection surface, internal noise of thermal camera, etc. Because of the relatively low temperature increase for AMT measurements of CFRP materials (on the order of 30 – 300 mK for the current CFRP sample), the level of noise is expected to be nontrivial relative to the thermal contrast caused by defects. To quantify and evaluate the effect of noise on the measurement results, the signal-to noise (SNR) is defined as [23]

$$SNR(t) = 10\log_{10}\frac{TC^2(t)}{\sigma_S^2(t)} \tag{11}$$

where $\sigma_S{}^2$(t) is the noise power (variance of temperature distribution over sound area) and is calculated as

$$\sigma_S^2(t) = \langle[\Delta T(x,y,t) - \langle\Delta T(x,y,t)\rangle_S]^2\rangle_S \tag{12}$$

In Figure 10, the SNR for three different FBHs is shown as a function of time. As expected, the SNR in Figure 10 is higher for the FBHs with larger *r* or smaller *d* due to higher level of TC. More importantly, this quantity experiences a considerable rate of change during the first 60 sec of microwave excitation. In addition, the SNR (in all cases) saturates (i.e., reaches an asymptotic value) after ~120 sec of microwave excitation. With this in mind, there is a maximum effective heating time of ~120 sec after which continued excitation does not improve the SNR. Therefore, the optimum (fastest inspection without loss of quality) inspection time can be considered ~120 sec for this application.

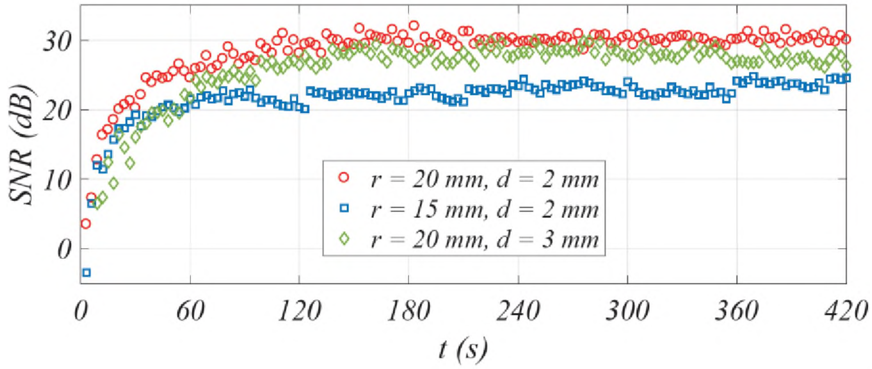

Figure 10. Signal-to-noise ratio for three FHBs with dimensions given in the figure legend

The SNR as defined in Eq. (11) uses the thermal contrast between defective and sound areas to evaluate the signal level. The SNR can also be considered from an image point-of-view (i.e., similar to the thermal images of Figure 7) in order to observe its saturation and evaluate the noise level throughout the inspection surface. Thus, the SNR over the whole inspection surface may be defined as:

$$SNR(x,y,t) = 10\log_{10}\frac{[\Delta T(x,y,t) - \langle \Delta T(x,y,t)\rangle_S]^2}{\sigma_S^2(t)} \qquad (13)$$

Using Eq. (13), SNR images are presented in Figure 11 for three different excitation times. As can be seen in Figure 11, the defective area appears after only an excitation time of ~30 sec due to the steep increase in the signal (TC) level relative to noise shown in Figure 10.

Also, the SNR saturation evident in Figure 11 can also be observed here by comparing the images at 120 and 420 sec. In other words, the equivalence of the images at 120 and 420 sec illustrates the SNR saturation and subsequently the maximum effective heat time.

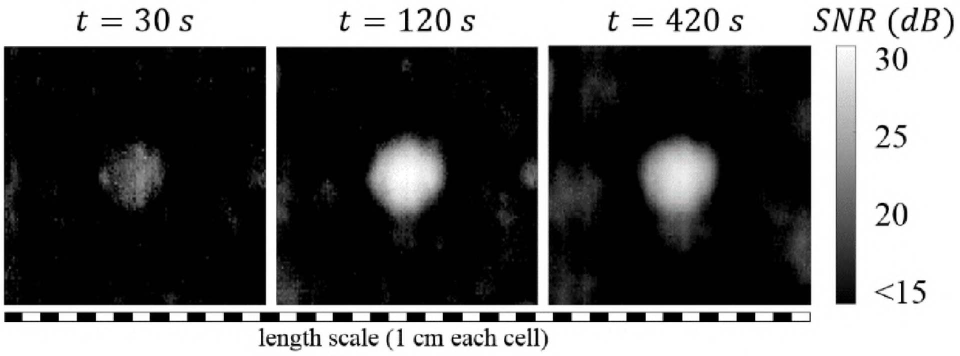

Figure 11. Signal-to-noise ratio image for FBH with $r = 20$ mm and $d = 2$ mm at different instants of time

4. CONCLUSION

Active microwave thermography (AMT) is an integrated nondestructive testing tool with strong potential in numerous aerospace and infrastructure applications. To this end, this work considers AMT as a potential inspection approach for detection of flat-bottom hole (FBH) defects in conductive composites (specifically, CFRP). Specifically, the effect of radius and depth, or combined as radius-to-depth ratio of FBH on its detection likelihood was studied through simulation and measurement. By considering the thermal contrast (i.e., difference between the temperature increase of a defective area and that of a sound/healthy area), it has been shown that detection likelihood can be improved by increasing the operating frequency of the microwave excitation or power level. AMT measurements were conducted for a number of FBHs machined in a multidirectional CFRP sheet showing practical possibility of detecting defects in conductive composites. The results showed that TC is independent of polarization selection for multidirectional (unlike unidirectional) CFRP due to its in-plane symmetrical structure. Ultimately, monitoring the signal-to-noise ratio (SNR) over time showed that a high level of defect information relative to background noise (>20 dB) is achievable after ~60 sec of microwave excitation, and a maximum effective heat time of 120 sec.

FUNDING DATA

Division of Electrical, Communications and Cyber Systems National Science Foundation under (Grant No. 1609470).

REFERENCES

[1] Zoughi, R., 2000, Microwave non-destructive testing and evaluation principles, vol. 4, Kluwer, Dordrecht, The Netherlands.

[2] Mirala, A., and Sarraf Shirazi, R., 2017, "Detection of surface cracks in metals using time-domain microwave non-destructive testing technique," IET Microw. Antennas Propag., 11(4), pp. 564-569.

[3] Ricci, M., Senni, L., and Burrascano, P., 2012, "Exploiting pseudorandom sequences to enhance noise immunity for air-coupled ultrasonic nondestructive testing," IEEE Trans. Instrum. Meas., 61(11), pp. 2905-2915.

[4] Abou-Khousa, M. A., Ryley, A., Kharkovsky, S., Zoughi, R., Daniels, D., Kreitinger, N. Steffes, G., 2006, "Comparison of X-Ray, Millimeter Wave, Shearography and Through-Transmission Ultrasonic Methods for Inspection of Honeycomb Composites," Proc. Rev. Prog. Quantitative Nondestr. Eval., 11(26B), pp. 999-1006.

[5] Ibarra-Castanedo, C., and Maldague, X., 2013, “Infrared thermography,” Handbook of Technical Diagnostics, Springer-Verlag Berlin Heidelberg, pp. 175-220.

[6] Poudel, A., Mitchell, K. R., Chu, T. P., Neidigk, S., and Jacques, C., 2016, “Non-destructive evaluation of composite repairs by using infrared thermography,” Journal of Composite Materials, 50(3), pp. 351-363.

[7] Yang, R., and He, Y., 2016, “Optically and Non-optically Excited Thermography for Composites: A Review,” Infrared Physics & Technology, 75, pp. 26-50.

[8] Balageas, D., and Levesque, P., 2002, “Mines detection using the EMIR method,” Proc. QIRT, pp. 71-78.

[9] DiMarzio, C. A., Rappaport, C. M., Li, W., Kilmer, M. E., and Sauermann, G. O., 1999, “Microwave-enhanced infrared thermography,” Proc. SPIE, Photonics, Photonics East (ISAM, VVDC, IEMB), pp. 337-342.

[10] Keo, S., Defer, D., Breaban, F., and Brachelet, F., 2013, “Comparison between microwave infrared thermography and CO_2 Laser infrared thermography in defect detection in applications with CFRP,” Mater. Sci. Appl., 4(10), pp. 600-605.

[11] Foudazi, A., Ghasr, M. T., and Donnell, K. M., 2015, “Characterization of corroded reinforced steel bars by active microwave thermography,” IEEE Trans. Instrum. Meas., 64(9), pp. 2583-2585.

[12] Foudazi, A., Mehdipour, I., Donnell, K. M., and Khayat, K. H., 2016, “Evaluation of steel fiber distribution in cement-based mortars using active microwave thermography,” Mater. Struct., 49(12), pp. 5051-5065.

[13] Foudazi, A., Edwards, C. A., Ghasr, M. T., and Donnell, K. M., 2016, “Active Microwave Thermography for Defect Detection of CFRP-Strengthened Cement-Based Materials,” IEEE Trans. Instrum. Meas., 65(11), pp. 2612-2620.

[14] Foudazi, A., Ghasr, M. T., and Donnell, K. M., 2014, “Application of active microwave thermography to inspection of carbon fiber reinforced composites,” Proc. IEEE AUTOTESTCON, pp. 318-322.

[15] Foudazi, A., Donnell, K. M., and Ghasr, M. T., 2014, “Application of active microwave thermography to delamination detection,” Proc. IEEE Int. Instrum. Meas. Technol. Conf. (I2MTC), pp. 1567-1571.

[16] Beemer, M. F., and Shepard, S. M., 2017, “Aspect ratio considerations for flat bottom hole defects in active thermography,” Quantitative InfraRed Thermography Journal.

[17] Paul, C. R., 2006, Introduction to Electromagnetic Compatibility, 2nd ed. Wiley, New York, Chap. 10.

[18] Lienhard IV, J. H., and Lienhard V, J. H., 2017, A Heat Transfer Textbook, 4th ed., Philogiston, Cambridge, Massachusetts, USA.

[19] Tian, T., 2011, “Anisotropic Thermal Property Measurement of Carbon-fiber/Epoxy Composite Materials,” Ph.D. dissertation, Dept. Mech. & Mater. Eng., Univ. Nebraska-Lincoln, Lincoln, NE, USA.

[20] Turi, E. A., 1997, Thermal Characterization of polymetric Materials, 2nd ed., Academic Press, San Diego, California, USA.

[21] Pletcher, R. H., Tannehill, J. C., and Anderson, D. A., 2012, Computational Fluid Mechanics and Heat Transfer, 3rd ed., CRC Press.

[22] Occupational Safety and Health Administration (OSHA) nonionizing radiation regulations, https://www.osha.gov/pls/oshaweb/owadisp.show_document?p_table=STANDARDS&p_id=9745.

[23] Meola, C., Carlomagno, G. M., 2004, “Recent advances in the use of infrared thermography,” Meas. Sci. Technol., 15(9), pp. 27-58.

II. ACTIVE MICROWAVE THERMOGRAPHY TO DETECT AND LOCATE WATER INGRESS

ABSTRACT

This paper reports on the application of a new and efficient nondestructive testing and evaluation (NDT&E) technique referred to as active microwave thermography (AMT) used to detect and locate water ingress within a structure. First, a mathematical formulation and analysis is established that relates the water extension and location to the temperature distribution over the inspection surface and enables evaluation of water from the measured temperature data. Following the analysis, AMT measurement results of a small volume of water, placed in a rubber sample at a predetermined location, are reported. The results verify the analysis and demonstrate the potential of AMT for water detection. Additionally, analysis of the measurement data indicates the potential of AMT for not only detection of water ingress, but also accurate depth estimation of small amounts of water ingress.

1. INTRODUCTION

Fluid absorption or the existence of undesired fluid, especially water ingress, may degrade the mechanical performance of composites and lead to structural failure [1]-[6]. Also, leakage from buried parts of water distribution networks and reservoirs can result in a serious amount of lost water [7]-[14]. Therefore, several nondestructive testing and evaluation (NDT&E) techniques are already employed to detect and locate the water ingress in composites and civil structures such as glass-fiber-reinforced polymer (GFRP) composites, aerospace honeycomb structures, and buried pipes. These techniques include infrared (IR) thermography, electromagnetic and microwave methods, ground penetrating radar (GPR), and acoustic methods [1]-[14].

Active microwave thermography (AMT) is a relatively new NDT&E method which has shown strong potential in detection and evaluation of various defect types such as crack, void, and delamination that impact composites and infrastructure [15]-[24]. This paper extends the spectrum of AMT applications to include detection and evaluation of water ingress. In AMT, a microwave signal of medium power (in the order of tens of watts) is radiated towards the inspection surface of the structure under test. For dielectric structures and depending on the structure's electromagnetic properties, a portion of the incident microwave energy penetrates the structure. Generally speaking, dielectric materials are described by their complex permittivity (often expressed relative to that of free-space, $\varepsilon 0$) as $\varepsilon_r = \varepsilon_r' - j\varepsilon_r''$ where ε_r' (or dielectric constant) represents the ability of a dielectric material to store microwave energy, and ε_r'' (or loss factor) represents the ability of a material to absorb energy. Dielectric heating results from absorption of microwave energy in lossy dielectric materials. Thus, when a lossy dielectric is irradiated with microwave energy, dielectric heating occurs as a result of the absorbed energy. As it relates specifically to this work, in the case where there is water (a lossy dielectric) ingress within a structure, the water will interact with the penetrating microwave radiation and convert this energy into heat (i.e., thermal energy), resulting in dielectric heating. This is different from Joule heating, which takes place in conductors exposed to electromagnetic radiation.

While this microwave-based heat generation takes place everywhere in the structure, it will be greater in the water than in the background material, as the loss factor of water is substantial [25]. Therefore, the area of the structure undergoing water ingress acts as a non-uniform volumetric heat source. Moreover, the amount of heat generated in the water depends on its volumetric distribution within the structure and the interrogating microwave energy parameters such as its strength (power level) and frequency. Subsequently, the generated heat diffuses inside the structure and reaches the inspection surface, where it causes a non-uniform temperature distribution that is greater in areas near the water ingress. Like other thermographic techniques, the inspection surface in AMT is monitored via a thermal camera which enables measurement of the temperature distribution. Spatial and temporal variations of the temperature distribution then are analyzed in order to obtain information regarding the water ingress. This information may include approximate volume and extension of the water ingress and its depth. As it relates to depth determination, often an approximate cross-sectional extension of the defect can be easily and directly identified in thermal images (generally speaking for thermographic techniques). However, evaluation of the depth of a defect often requires complex analysis on the temporal evolution of the thermal images, as is the case in this work.

In general, AMT has several advantages including short inspection times for relatively large areas, non-contact interrogation and inspection, and easy-to-interpret results (results are obtained in an image format and can be visually interpreted to some extent). Beside these advantages that AMT shares with other thermographic methods [26], microwave radiation as the thermal excitation is particularly well-suited for detection of water ingress due to the fact that water is highly absorptive to electromagnetic energy in the microwave frequency range [25]. In fact, AMT offers the advantage of selective heating as the heat source is exerted only upon the defect (water ingress), with less interaction with the background material. In this case, unlike conventional thermography, the defect acts as a heat source, rather than merely affecting the heat diffusion. As such, AMT is uniquely effective and potentially superior to other thermographic methods.

In this research, microwave radiation at 2.4 GHz is utilized because water has a high absorption of microwaves at this frequency. Further, this frequency is in the license-free industrial, scientific and medical (ISM) radio band. Measurement results are provided in Section III, after the modeling results of Section II, that show a high efficacy of AMT for water detection and validate the relevant formulation and analysis provided next.

2. MODELING AND THEORY

2.1. BASIC FORMULATION

As mentioned, the temperature distribution over the surface of structure is measured in an AMT inspection and used to extract information regarding defects within the structure. The relationship between the defect (water ingress) acting as a heat source, Q, and the temperature distribution induced by this source, T, can be established by the heat equation as [27]:

$$\left(\frac{\partial}{\partial t} - \alpha\nabla^2\right)T = \frac{1}{\rho c}Q \tag{1}$$

where α, ρ, and c denote the thermal diffusivity, density, and the specific heat capacity of the structure in which heat diffuses, respectively. In other words, the heat equation of (1) relates the temporal and spatial variation of temperature to the heat source and material properties. In addition, in this paper, the temperature (*T*) refers to the temperature increase caused by the water ingress, and does not reflect the initial temperature distribution or the temperature rise caused by the background material (structure).

To find the temperature distribution from (1), the model shown in Figure 1 is used. In this model, the structure is assumed as a half-space located at $z \leq 0$ and contains water ingress of volume, *V*. Moreover, the *x*- and *y*-axes represent cross-sectional coordinates, and the *z*-axis (positive *z*) points toward the structure depth, with the inspection surface located at $z = 0$. Using the Green's function method as detailed in [28], the solution to (1) can be written as:

$$T(x,y,t) = \frac{1}{\rho c}\iiint_V G(x,y,t|x',y',z') * Q(x',y',z',t)dV' \tag{2}$$

This equation relates the temperature over the inspection surface at point (x,y) to the heat source distribution located at (x',y',z') at any time. In addition, $dV' = dx'dy'dz'$ is the heat source's element of volume, and G denotes the Green's function and has the closed form of

$$G(x,y,t|x',y',z') = \frac{1}{4\sqrt{\pi\alpha t}^3} exp\left[-\frac{(x-x')^2+(y-y')^2+z'^2}{4\alpha t}\right] \tag{3}$$

for the model of Figure 1 when the thermal boundary condition is assumed to be adiabatic on the inspection surface. For controlled environments and small temperature increases over the structure surface (as in AMT), this assumption is very accurate since the air is steady above the surface and has a low temperature difference with the surface.

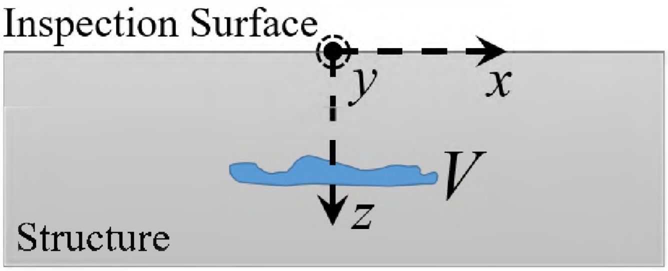

Figure 1. Basic model used to formulate and analyze water detection using AMT

In order to use (2) to determine the surface temperature distribution (*T*), the thermal source's power density (*Q*) as a function of space and time must be known. In AMT, the microwave excitation is continuously applied for a certain time, referred to as heating time (denoted by τ). In addition, the cooling period starts when the microwave excitation is removed. Therefore, the power density due to the dielectric heating may be written as:

$$Q(x,y,z,t) = \begin{cases} \pi f \varepsilon_0 \varepsilon_r'' E^2 & 0 < t \leq \tau \\ 0 & otherwise \end{cases} \tag{4}$$

where f, ε_r'', and E are the microwave frequency, dielectric loss factor of water, and the magnitude of the incident electric field in the water, respectively. The complex permittivity of water at 2.4 GHz and room temperature is $77 - j9$ [25]. This value remains constant throughout this research because the frequency is fixed and the temperature change does not exceed 4 °C. As mentioned earlier, high value of water's dielectric loss factor results in high absorption of microwave energy by water, thereby enabling water ingress detection by AMT efficiently. In addition, the value of E depends on many factors including the incident microwave power density, material properties of the background structure (here, rubber), and the location and distribution of the water ingress.

A closed form solution to (2) cannot be obtained in most cases due to the complexity of the integrals and the convolution operator within the integrals. Hence, it is often numerically evaluated. However, a closed form solution for the temperature distribution over the structure surface can be calculated from (2) for an infinitesimal volume of water, V, located at $(0,0,d)$, and is given as:

$$T(r,t) = \frac{Q_0 V}{2\pi k r}\left[erf\left(\frac{r}{\sqrt{4\alpha(t-\tau)u(t-\tau)}}\right) - erf\left(\frac{r}{\sqrt{4\alpha t}}\right)\right] \tag{5}$$

where $k = \alpha\rho c$ is the thermal conductivity of the structure and $r = \sqrt{x^2 + y^2 + d^2}$ is the distance from the water ingress to the measurement point on the surface. Also, $Q_0 = \pi f \varepsilon_0 \varepsilon_r'' E^2$, which is, generally speaking, a function of water ingress distribution (i.e., its volume). However, this quantity is independent of volume when V is infinitesimal such that the scattering of the microwave fields by the water ingress be insignificant and the electric field be considered constant within the entire water volume. This condition requires the water to be thinner than approximately one-tenth of the wavelength of the microwave in the water [29] (in this case, approximately 1.4 mm). As a result, the temperature is a linear function of volume according to (5) for infinitesimal V.

2.2. SIMULATIONS

To verify the formulation of (5) and investigate the effect of water ingress depth on temperature, an AMT test to detect a small rectangular volume of water with $V = 0.05$ mL, equal to volume of an average water drop [30], is simulated and compared with the temperature as calculated using the analytical expression of (5). Specifically, full wave simulations are conducted using a coupled electromagnetic/thermal model created using CST Microwave Studio and Multiphysics Studio software packages. The simulated structure consists of a piece of rubber exposed to 300 seconds of microwave radiation with 50 W incident power at 2.4 GHz. The water ingress is placed at depths of 6, 9, and 12 mm. The electromagnetic and thermal properties of water and rubber are given in Table 1, and the simulated results are given in Figure 2 as a function of time and position on the structure surface (cross-sectionally above the location of water ingress).

Table 1. Properties of water and rubber [25],[31],[32]

Material	**Property**	**Value**
Water	Dielectric Constant (ε_r)	77
	Dielectric Loss Factor (ε_r'')	9
Rubber	Dielectric Constant (ε_r)	2.4
	Thermal Diffusivity (α)	0.11 mm^2/s
	Thermal Conductivity (k)	0.16 W/m·K

In Figure 2(a), temperature on the rubber surface above the location of water ingress is shown versus time. As expected, the temperature rises during the heating period and reduces during the cooling period. The temperature decay has a delay from the cooling period start-point (i.e., $t = 300\ s$) which is a function of water depth, as is discussed later. Also, the absolute temperature values are highly affected by the depth of water. That is to say, the maximum temperature increase for the cases with depths of 6, 9, and 12 mm is 1.56, 0.66, and 0.32 °C, respectively. In addition, as the thermal camera used in this work has a temperature sensitivity of 0.03 °C, shown by the green line in Figure 2(a), detection of very small volumes of water (one drop, in the current case) is possible after a few minutes. More specifically, a heating period of 1 minute is sufficient for detection of a drop at a depth of up to 15 mm, 4 minutes for detection up to 25 mm, and a 10-minute inspection can theoretically detect this volume of water at a maximum depth of 34 mm.

In Figure 2(b), the temperature distribution on the structure surface is shown versus position over the water ingress. As seen, when the heat source (water ingress) is located deeper in the structure, the temperature curves have wider spatial distributions. In fact, the thermal energy spreads more extensively before reaching the surface for larger depths. As a result, the spatial temperature distribution is better confined to the corresponding physical distribution when the source is closer to the surface and therefore is a better indication of the cross-sectional extension of water. This will also be shown in the next section with the results of experimental AMT tests.

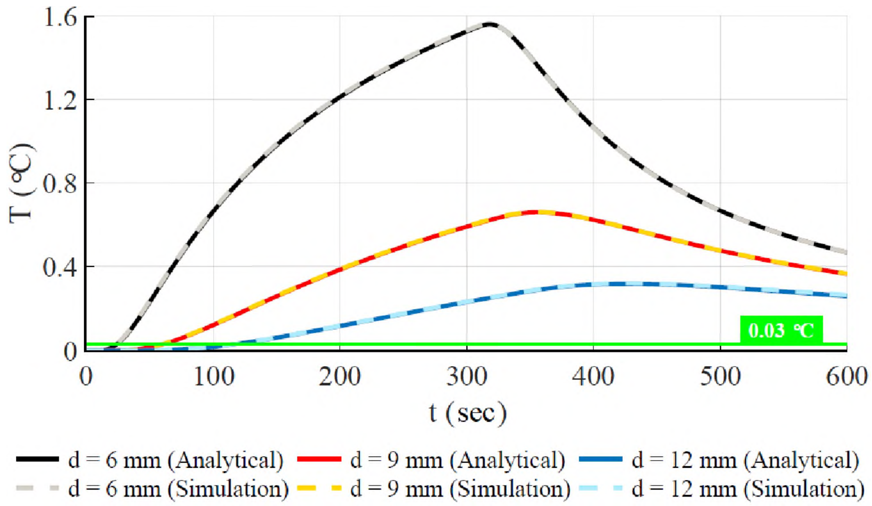

(a)

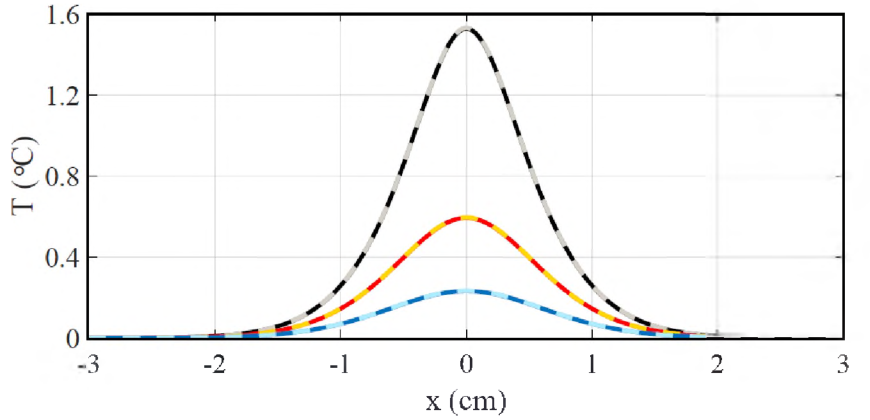

(b)

Figure 2. Temperature versus time (a) and position over the structure surface (b) for 0.05 mL water ingress at depths of 6, 9, and 12 mm, calculated analytically and by coupled electromagnetic/thermal simulations

In Figure 3, a 3D representation of the distribution of the stored thermal energy density (in J/cm^3) generated by microwave heating, inside and over the surface of the structure, is shown for the case of d = 9 mm at t = 180, 360, and 540 sec. This quantity is calculated by the proposed analytical formulation and the equation $q = \rho c T$ [27]. As shown, the thermal energy is highly concentrated at and around the location of water ingress during the heating period, as shown for *t* = 180 sec. As the time increases (i.e., *t* = 360 sec), a significant amount of thermal energy has reached to the surface of the sample and the temperature on the sample surface is maximum (see Figure 2a). During the cooling period, on the other hand, heat diffuses further into the sample away from the location of water ingress, as can be seen at *t* = 540 sec.

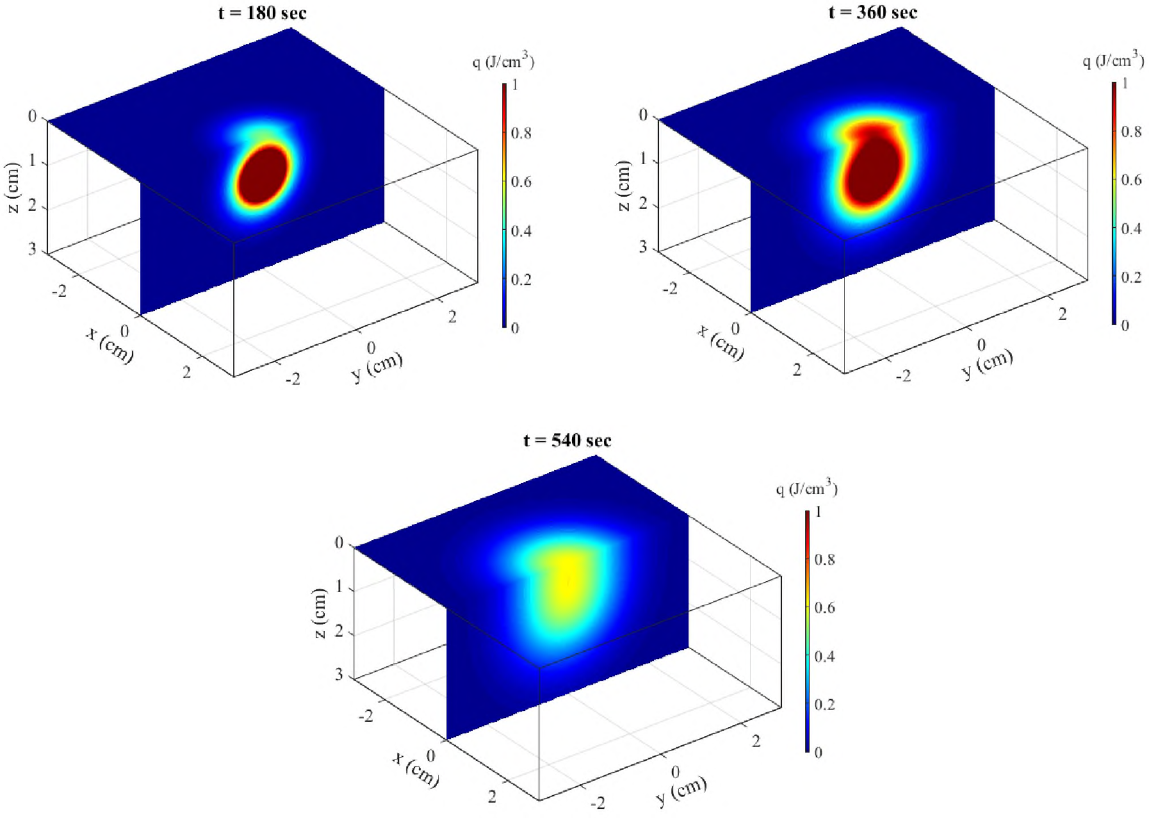

Figure 3. 3D distribution of stored thermal energy for water ingress with *d* = 9 mm at different instances of time

For a better observation of the dependence of temperature on depth, the maximum value of temperature is calculated by (5) for different values of *d* and τ for the same microwave power, water volume, and structure as given before, with the results depicted in Figure 4. Specifically, in Figure 4(a), the maximum temperature is calculated for depths of 5-15 mm with the heating time ranging from 1-10 min. As seen, the temperature highly depends on the depth and exponentially decreases for larger depths. This leads to reduced detectability of the water since detectability of a defect depends on the induced surface temperature along with the sensitivity of the thermal camera [15]. Moreover, the temperature and subsequent detectability increases with the heating time, as expected. This, however, requires longer inspections. More specifically, for deeper defects, the temperature may have a maximum that is below the temperature measurement sensitivity, as shown in Figure 4(b), where the maximum temperature is shown for depths of 20-50 mm. For a thermal camera with a sensitivity of 0.03 °C (as is used for this work), water ingress that yields a temperature less than this value are undetectable, as indicated in the figure. For example, with a heating time of 300 sec, the maximum depth for a detectable defect is 27 mm, but this value is 34 mm if the heating time is 600 sec. These values are for the specific structure, microwave excitation, and water ingress distribution as are given here and must be recalculated for different inspection scenarios. In addition, as is apparent in Figure 4 (both), the temperature does not monotonically grow with the heating time and the curves of high τ asymptotically approach a limit. More specifically, in the limit of infinite heating time, (5) reduces to $T_{\max} = Q_0 V/2\pi kd$. By considering a theoretical detectability criteria defined as $T_{\max} > S$, where S is the sensitivity of the thermal camera, a relationship between depth and sensitivity can be defined as $d < Q_0 V/2\pi kS$. For the parameters used here, a defect deeper than 669 mm is (theoretically) undetectable, even with an infinitely long heating time, according to this relation. This relation also indicates an inverse proportionality between detectable depth and the structure's background material's thermal conductivity. This means that AMT is more efficient in detection of water in structures with lower thermal conductivities, while in conventional thermographic techniques, the difference between thermal conductivities of the structure and the defect is important [33]. This may make AMT superior to conventional thermography for structures with a thermal conductivity close to that of water. In addition, it should be noted that one way to increase the induced heat is to employ a higher frequency or microwave excitation power as $Q_0 \propto f\,E^2$. However, increasing the power level and frequency both increase system cost along with regulatory and safety limits that may be imposed [15].

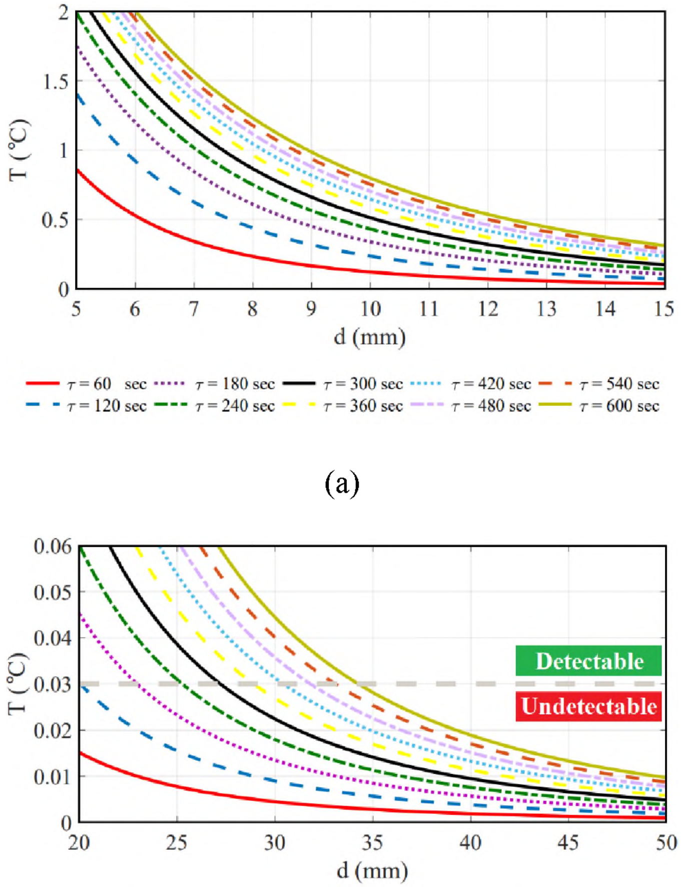

(a)

(b)

Figure 4. Maximum of temperature vs. depth for different values of heating time

2.3. DEPTH EVALUATION

According to Figure 2, beside the impact of depth on the maximum value of temperature increase, for a deeper water ingress, the rate of temperature change is less than that of shallower ingress in both the heating and cooling periods. In addition, the transition between the increasing and decreasing temperature takes place at a later time (relative to the shallower depths). In fact, for near-surface water ingress, the temperature reaches its maximum at the end of heating time and starts decreasing immediately in the cooling period, while, due to the distance between the water and the inspection surface for deeper water ingress, the temperature maximum occurs with a delay, Δt with respect to τ. This concept is illustrated in Figure 5. Moreover, this delay, which can be measured in any AMT inspection, can be used to estimate the depth of water ingress inside the structure. Based on this, as the rate of change of T with respect to time is zero at the maximum of T, the equation $\partial T/\partial t|_{t=t_0} = 0$ is considered to find the relation between $t_0 = \tau + \Delta t$ and d. As the desired relation depends on the distribution of water ingress, a simple model shown in Figure 6(a) is used here. In this model, a very thin rectangular layer of water with height, h, and cross-sectional dimensions, ℓ and w, is placed in a depth of d inside the structure. The heat source then is considered as

$$Q = \begin{cases} Q_0 h\delta(z-d) & |x| \le \frac{\ell}{2}, |y| \le \frac{w}{2}, 0 < t \le \tau \\ 0 & otherwise \end{cases} \tag{6}$$

Using (2) and (6) and applying $\partial T/\partial t = 0$, the depth can be found as:

$$d = \sqrt{\frac{4\alpha t_0 \Delta t}{\tau} ln\left(\sqrt{\frac{t_0}{\Delta t}} \frac{erf(\ell/4\sqrt{\alpha\Delta t})erf(w/4\sqrt{\alpha\Delta t})}{erf(\ell/4\sqrt{\alpha t_0})erf(w/4\sqrt{\alpha t_0})}\right)} \tag{7}$$

which can be used once the length and width of water ingress is estimated from the thermal images. As it relates to practical inspections, in many cases, ingressed water distributions are of the special forms shown in Figure 6(b): extended (when water ingress has a large cross-sectional area), linear (such as water seeped into a crack or vein), and point (like drops) [34]. In all of these cases, (7) can be simplified as:

$$d = \kappa \sqrt{\frac{2\alpha t_0 \Delta t}{\tau} ln\left(\frac{t_0}{\Delta t}\right)} \tag{8}$$

where $\kappa(\ell, w \to \infty) = 1$, $\kappa(\ell \to \infty, w \to 0) = \sqrt{2}$ and $\kappa(\ell, w \to 0) = \sqrt{3}$, for extended, linear, and point distributions, respectively. Here, κ is a coefficient that depends on the cross-sectional extension of the water and is always $1 < \kappa < \sqrt{3}$. Using (8) for the three cases of Figure 2 with t_0 = 319, 357, and 427 sec (extracted from the curves in Figure 2) yields exact values for ingress depths of 6, 9, and 12 mm (the precise values used in simulation above). The formulation given in this section, therefore, is validated by comparing the results of (8) to the simulation results obtained from commercial software CST Microwave Studio and Multiphysics Studio.

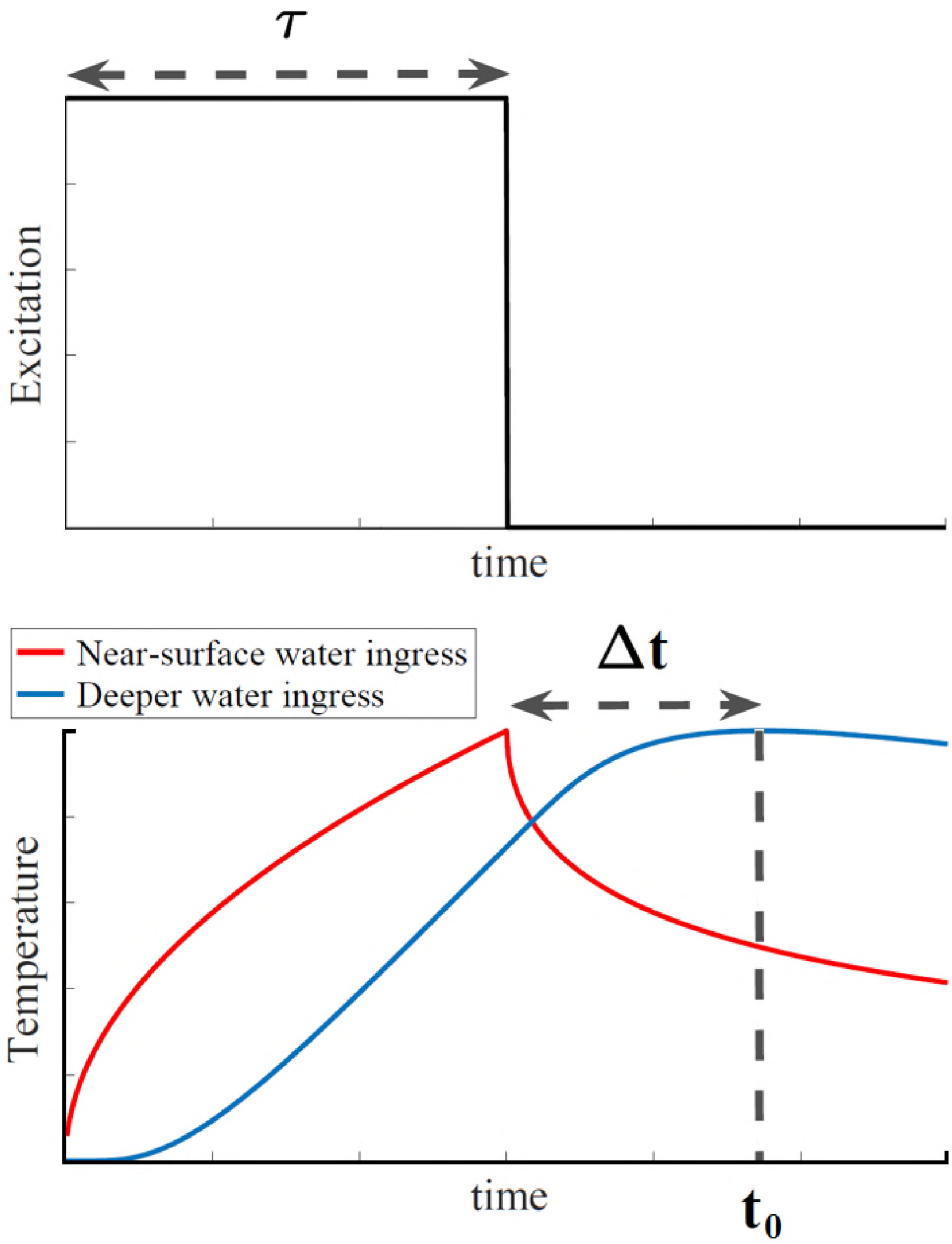

Figure 5. The microwave excitation pulse shape and temperature response to this excitation for near-surface and deeper water ingress cases

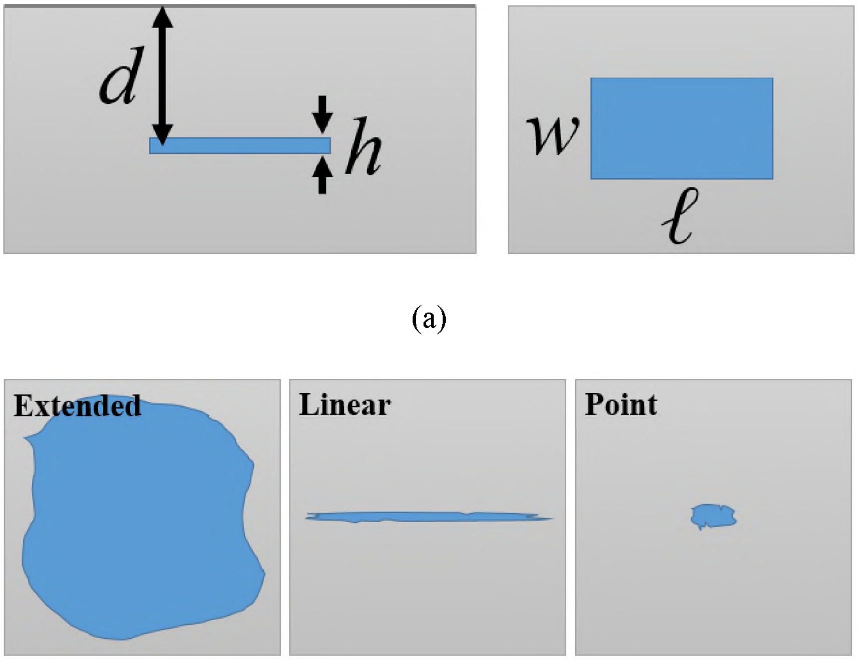

(a)

(b)

Figure 6. (a) Rectangular model used to study the relation between water depth and the delay time, Δt, and (b) special water distributions

2.4. EFFECT OF BACKGROUND MATERIAL

For the simulation results provided in the previous sections and measurements provided in the next section, rubber, as a representative material within which water ingress may occur, was assumed to be the background material. Detection of water ingress in rubber finds application in inspection of submarine acoustic tiles [35], heavy electrical component insulators [36], sealed cabins of aircraft and ships as well as in high-temperature and high-pressure water and oil seal rings [37]. The application of AMT for water ingress detection, however, is not limited to rubber and can be considered for any material which allows microwave energy to penetrate. This includes a variety of materials such as GFRP, honeycomb, and mortar. For good electrical conductors and dielectrics with significant loss, the application of AMT for detection of water ingress will be very limited, since the microwave energy does not penetrate the surface and hence will not reach the water. Therefore, in order to study the effect of background material properties on the efficacy of AMT, a number of simulation results are presented here.

In general, permittivity (ε_r), thermal diffusivity (α), and thermal conductivity (k) are the parameters which fully characterize the background material's effect on the thermal response of water ingress. These parameters are given for GFRP, HRH-10 honeycomb, and mortar in Table 2. The HRH-10 honeycomb is a dielectric honeycomb structure which is widely used throughout the aerospace industry, as most of the interior panels of commercial jets and exterior aircraft parts such as radomes, fairings, helicopter blades, flaps, etc., are made with this material [40]. As this structure is a very low-loss dielectric, AMT is expected to easily detect water ingress trapped within its cells.

Table 2. Materials properties [38]-[41]

Material	ε_r	**α (mm^2/s)**	**k (W/ m·K)**
Rubber	2.4	0.11	0.16
GFRP	$3.5 - j\,0.07$	0.26	0.43
Honeycomb	1.1	1	0.07
Mortar	$4.8 - j\,0.05$	0.6	1.2

The thermal response to the microwave excitation is given in (5) and was evaluated for rubber, as shown in Figure 2. For the same case shown in Figure 2 (V = 0.05 mL and d = 9 mm) but with different background materials, the temperature versus time is depicted in Figure 7. As seen in this figure, different materials render different responses to AMT. Specifically, for rubber, GFRP, honeycomb, and mortar, the maximum of temperature occurs at different times with Δt = 57, 17, 3, and 5 sec, respectively. According to these values and also from (8), for a material with a lower diffusivity, the maximum temperature occurs at a later time. More importantly, the maximum values of temperature increase for the rubber, GFRP, honeycomb, and mortar are 0.66, 0.43, 2.26, and 0.20 °C, respectively. These values show how thermal conductivity of the background material affects the maximum temperature rise and thus the detectability of a defect. In fact, according to (5), for a constant α, the maximum temperature is inversely proportional to the thermal conductivity. Therefore, the low thermal conductivity of honeycomb (which is due to its low mass density [40]), the temperature has a much steeper increase and this results in a faster detection of water ingress. On the other hand, mortar is a weak thermal conductor and therefore the rate of temperature increase is reduced.

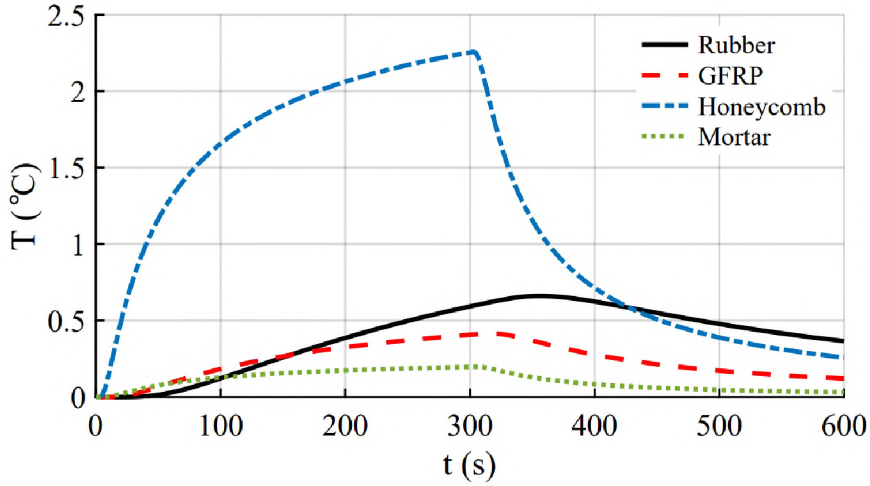

Figure 7. Temperature increase versus time for 0.05 mL of water ingress at a depth of 9 mm, calculated for different materials

For a better demonstration of the effect of background material properties on the maximum temperature increase and the time at which this maximum occurs, $T_{\max}$ and Δt are shown versus α and k when other parameters are constant ($\varepsilon_r = 2.4$, $V = 0.05$ mL, $d = 9$

mm, and τ = 300 sec), in Figure 8. As expected, Δt is smaller for higher values of α since a higher thermal diffusivity means that the heat diffuses faster in the materials and that shortens the time required for the heat to reach the sample surface. T_{max}, however, is a function of both α and k, and increases significantly for lower values of k. The effect of background material's thermal diffusivity and conductivity on thermal responses in AMT tests was shown in this section (in Figure 7 and Figure 8) and can be extrapolated to other materials when detection of water ingress is desired. It should be also noted that AMT's success is limited when background materials, such as conductive materials, do not allow penetration of microwave radiation into their depth.

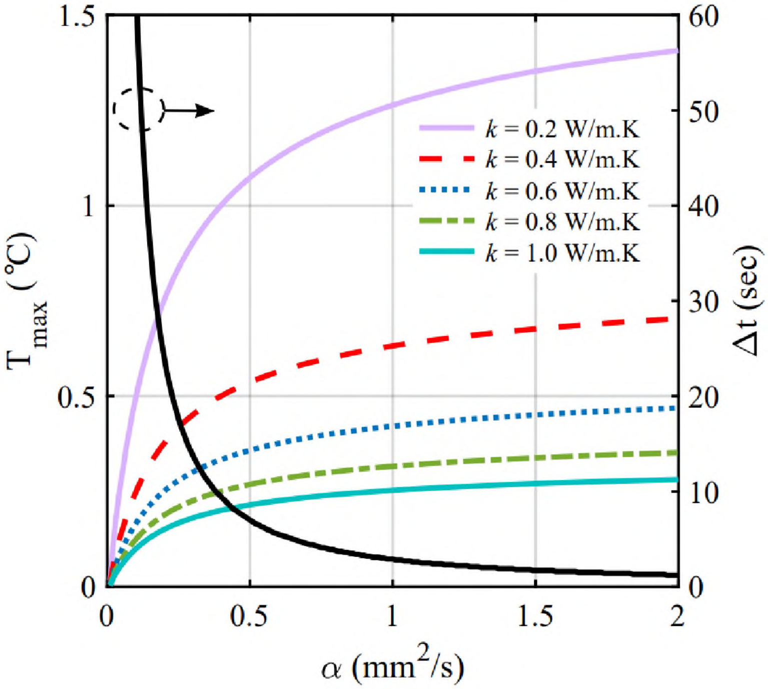

Figure 8. Maximum of temperature increase and Δt versus α and k

3. MEASUREMENTS

3.1. METHOD

The AMT system is depicted in Figure 9. The system consists of an RF source locked at 2.4 GHz and a 50 W microwave amplifier. A ridged horn antenna is used to direct the microwave radiation onto the structure surface. This antenna is capable of handling and radiating high-power microwave energy in the operational frequency range of 1-4 GHz with a gain of 14 dBi at 2.4 GHz. The antenna has a total length of 40 cm and aperture dimensions of 23×17 cm^2. A thermal camera (FLIR T430sc) with sensitivity and frame rate of respectively 0.03 °C and 30 Hz is used to measure the surface thermal profile of the structure. The thermal camera captures thermal images with a resolution of 320 × 240 pixels. The spatial resolution of the thermal images of the sample surface depends on the camera's field-of-view. In this work, thermal images have a resolution of 0.6×1.1 mm^2 over the sample's surface. The RF source, power amplifier, and thermal camera are controlled and synchronized by the control unit. The control unit consists of a data acquisition (DAQ) device which is controlled by the software package MATLAB. MATLAB's data acquisition and image acquisition toolboxes work simultaneously to control the microwave excitation and record thermal images.

The distance between the antenna and surface of the structure under test is referred to as the lift-off distance. For AMT inspections, the lift-off distance must be such that the incident power over the inspection area results in a measurable temperature increase but also allows viewing of the sample surface with the thermal camera. For this work, the lift-off distance is 13 cm for all measurements. The radiation from the horn antenna covers the region containing the defect that is located in the saturated paper towel. For cases where a large inspection area is needed, sections of the structure can be inspected individually by raster scanning, or by using an antenna, or multiple antennas with a wider radiation pattern. In any case, the analysis method and outcomes reported herein remain the same.

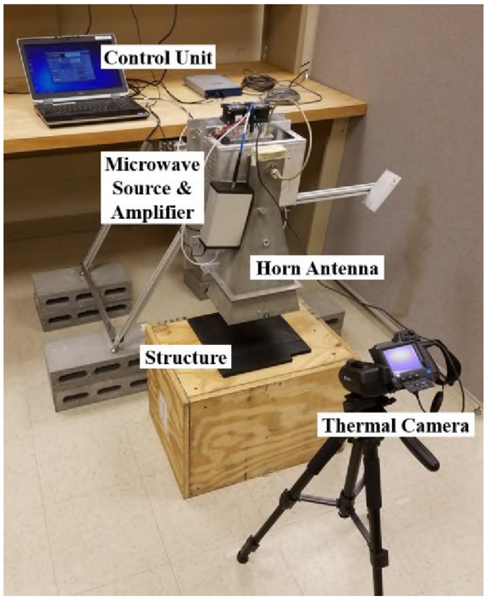

Figure 9. AMT system for water detection

3.2. RESULTS

A number of tests were performed using the AMT system as described above, to investigate the practical efficacy of AMT for water detection. The water was added to a 4×4 cm^2 piece of paper towel and the paper towel was sandwiched between a thick (2 cm) rubber sample at the bottom and thin (1-7 mm) layers of the same rubber at the top. The thickness of the top rubber layer is then considered as the depth of the water. Three different volumes of water, 0.5, 1, and 2 mL, were added to the paper towel and correspond to h = 0.3125, 0.6250, and 0.9375 mm, respectively. As a result, the water distribution was assumed to be that illustrated in Figure 6(a) (rectangular with dimensions ℓ, w, and h and depth d from the surface). The microwave excitation of 50 W at 2.4 GHz was applied for 300 sec, with an additional 300 sec of cooling time (i.e., a total test duration of 600 sec). Thermal images were recorded and post-processed in order to yield temporal and positional temperature behavior. Also, the initial thermal image at t = 0 sec is subtracted from all subsequent thermal images in order to obtain the temperature increase (considered above in the simulated and analytical results) instead of the absolute temperature. In Figure 10, the thermal images are shown for the cases of d = 1 and 4 mm and all three volumes at t = 120, 300, 330, and 600 sec. Dashed black lines over the thermal images show the physical cross-sections of water below the surface. As seen and expected, the temperature is greatest at a location centered on the location of water, and the hot area is considerably confined within the water boundaries. In addition, small volumes of water such as 0.5 mL are clearly detected after 120 sec of microwave heating. In addition, due to thermal diffusion, the temperature is not zero outside the boundaries, especially at latter instances of time. More specifically, the temperature becomes more uniform at t = 600 sec since by this time in the cooling period, the heat has diffused significantly to adjacent areas. Furthermore, it can be noted that for deeper water (4 mm depth), the temperature is more spread over the inspection surface, as was discussed and shown in Figure 2(b). This fact makes it harder to estimate the physical extension of deeper water, as the thermal images lose contrast.

Another important aspect seen in the thermal images of Figure 10 is that for the depth of 1 mm, the temperature is maximum at t = 300 sec, while it is maximum at t = 330 sec for the depth of 4 mm. In fact, the depth of 4 mm corresponds to t_0 = 326 sec as calculated by (8) for the maximum of the temperature, indicating good agreement between the theory above and measurement results.

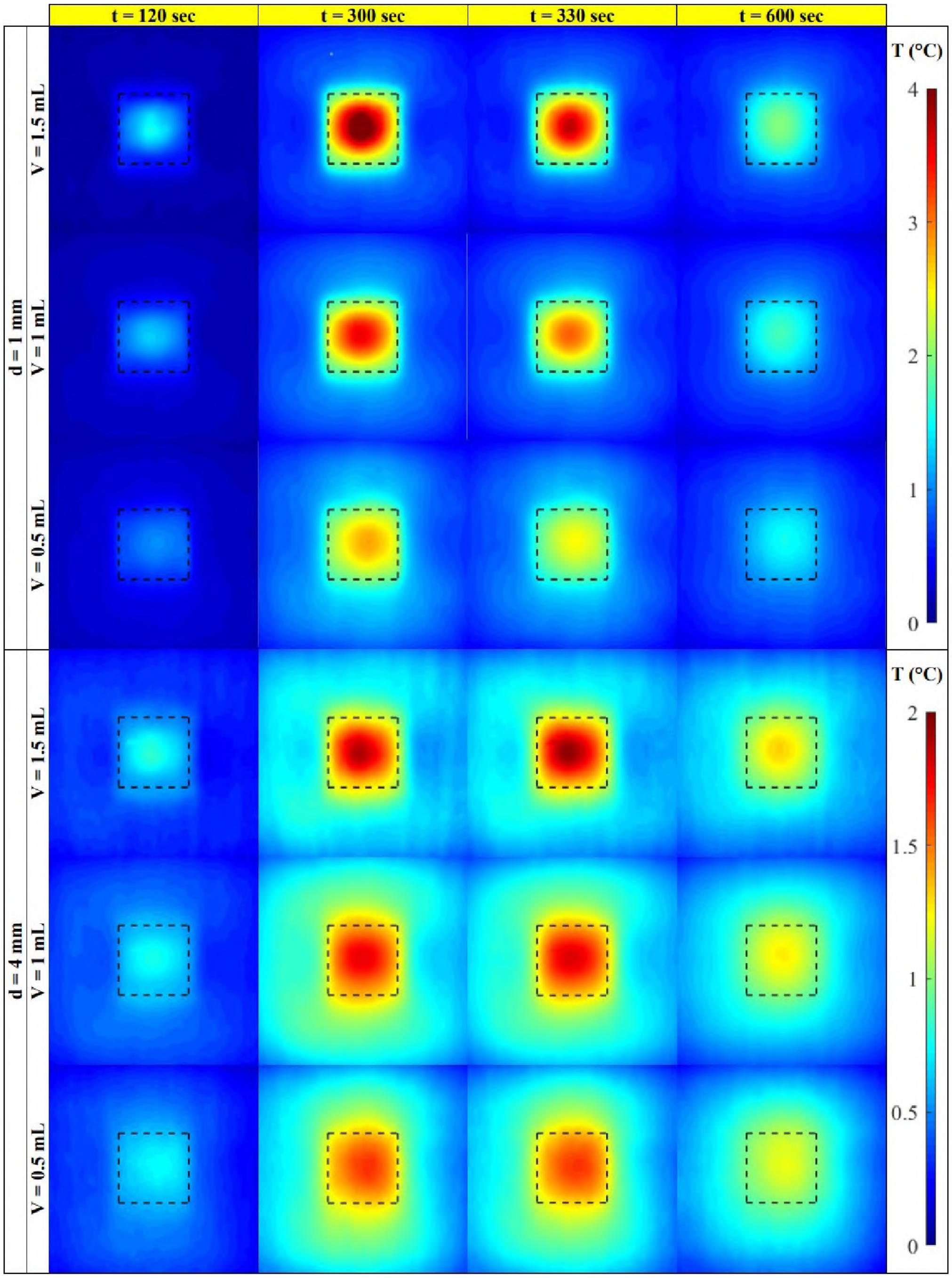

Figure 10. Thermal images related to different volumes and depths of water at different times obtained through AMT measurements

To further investigate the potential of AMT for evaluation of water depth, water was placed at depths of 1, 2.5, 4, 5.5, and 7 mm and the temporal evolution of temperature was monitored. The temperature was averaged over a square area (to reduce the effect of noise with respect to a single point) of 4×4 mm^2 centered on top of the water [15]. Figure 11 shows the temperature curves obtained through experiments as well as numerical evaluation of (2). Excellent accordance between the measured and numerically evaluated results is observed. More importantly, the measured delay, Δt, was used to estimate the depth of water from (8). Table 3 lists the measured t_0 and the corresponding depths calculated by (8). As seen, the calculated depth values are in good agreement with the actual depths and the relative error is small (~5% on average). The error can be due to noise from the environment, variations of sample emissivity and thermal properties, thermal camera intrinsic noise, etc. These results strongly support the potential of AMT as an efficient NDT&E technique for detection and evaluation of water ingress.

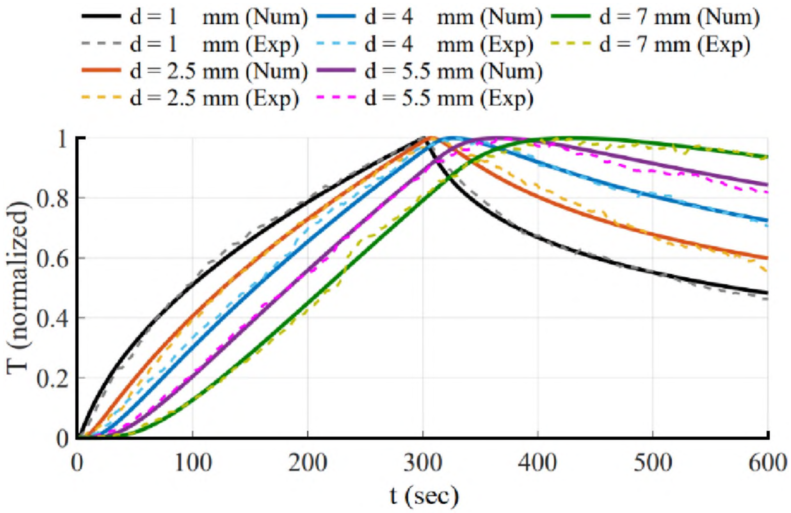

Figure 11. Experimental and numerical evaluation of temperature (normalized) caused by water ingress at different depths and the effect of depth on the temporal evolution of temperature curves

Table 3. Calculated depths of water and their errors

Actual d (mm)	**Measured t_0 (sec)**	**Calculated d (mm)**	**Error (%)**
1	301	1.1279	12.8
2.5	308	2.5897	3.6
4	330	4.2383	6.0
5.5	367	5.7069	3.8
7	420	7.2065	2.9

4. CONCLUSION

The potential of active microwave thermography (AMT) as an inspection tool for detection of ingressed water was assessed through mathematical analysis, simulations, and measurement. The results indicate that AMT has strong potential to detect and locate small volumes of water ingress after a few minutes of microwave excitation. Specifically, an amount of water on the order of a few drops was detected in a rubber sample at a depth of a few millimeters. More importantly, the depth of water was estimated using experimental data and mathematical formulation, with an average error of ~5%. To this end, a simple formulation was proposed to relate the temporal behavior of the temperature obtained through AMT measurements and the depth of the water. In addition, the relationship between the detectability of water and the test parameters such as the microwave excitation frequency and power, water volume and depth, structure properties, and the heating time was established.

REFERENCES

[1] L. Rocha, “Combined experimental/numerical investigation of directional moisture diffusion in glass/epoxy composites,” Composites Science and Technology, vol. 151, pp. 16-24, Oct. 2017.

[2] P. Wang, Y. Pei, and L. Zhou, Near-field microwave identification and quantitative evaluation of liquid ingress in honeycomb sandwich structures,” NDT&E International, vol. 83, pp. 23-37, Oct. 2016.

[3] P. Malinowski et al, “Moisture detection in composites by terahertz spectroscopy,” J. Phys.: Conf. Ser., vol. 628, iss. 1, pp. 012100, 2015.

[4] E. Barjasteh, and S. R. Nutt, “Moisture absorption of unidirectional hybrid composites,” Composites: Part A, vol. 43, Iss. 1, pp. 158-164, Jan. 2012.

[5] N. P. Avdelidis, A. Moropoulou, and P. Theoulakis, “Detection of water deposits and movement in porous materials by infrared imaging,” Infrared Physics & Technology, vol. 44, Iss. 3, pp. 183-190, Jun. 2003.

[6] G. Sala, “Composite degradation due to fluid absorption,” Composites: Part B, vol. 31, no. 5, pp. 357-373, Jul. 2000.

[7] D. Ayala-Cabrera et al., “GPR-Based Water Leak Models in Water Distribution Systems,” Sensors, vol. 13, no. 12, pp. 15912-15936, Nov. 2013.

[8] Z. Liu, Y. Kleiner, “State of the art review of inspection technologies for condition assessment of water pipes,” Measurement, vol.46, no. 1, pp. 1-15, Jan. 2013.

[9] A. Cataldo, G. Cannazza, E. De Benedetto, and N. Giaquinto, “A new method for detecting leaks in underground water pipelines,” IEEE Sensors J., vol. 12, no. 6, pp. 1660-1667, Jun. 2012.

[10] S. Demirci et al, “Ground penetrating radar imaging of water leaks from buried pipes based on back-projection method,” NDT&E International, vol. 47, pp. 35-42, Apr. 2012.

[11] T. Hao et al., “Condition assessment of the buried utility service infrastructure,” Tunneling Underground Space Technol., vol. 28, no. 1, pp. 331-334, Mar. 2012.

[12] E. Grinzato et al, “Infrared Thermography for Moisture Detection: A Laboratory Study and In-situ Test,” Materials Evaluation, vol. 69, Iss. 1, pp. 97-104, Jan. 2011.

[13] M. Fahmy, and O. Moselhi, "Automated detection and location of leaks in water mains using infrared thermography," J. Perform. Constructed Facilities, vol. 24, no. 3, pp. 242-248, Jun. 2010.

[14] M. Bimpas, A. Amditis, and N. Uzunoglu, "Detection of water leaks in supply pipes using continuous wave sensor operating at 2.45 GHz," Journal of Applied Geophysics, vol. 70, Iss. 3, pp. 226-236, Mar. 2010.

[15] A Mirala, A. Foudazi, M. T. Ghasr, and K. M. Donnell, "Detection of Flat-Bottom Holes in Conductive Composites Using Active Microwave Thermography," ASME J Nondestructive Evaluation, vol. 1, Iss. 4, pp. 041005-1-041005-7, Nov. 2018.

[16] A. Foudazi, A. Mirala, M. T. Ghasr, and K. M. Donnell, "Active Microwave Thermography for Nondestructive Evaluation of Surface Cracks in Metal Structures," IEEE Trans. Instrum. Meas., vol. 68, no. 2, pp. 576-585, Feb. 2019.

[17] A Mirala, X. Zou, M. T. Ghasr, L. Sneed, and K. M. Donnell, "Active Microwave Thermography: A Real-Time Monitoring Tool for CFRP-Concrete Bond Testing," in Proc. IEEE Int. Instrum. Meas. Technol. Conf. (I2MTC), May 2019, pp. 1-6.

[18] A Mirala, M. T. Ghasr, and K. M. Donnell, "Nondestructive assessment of microwave absorbing structures via active microwave thermography," in Proc. IEEE Int. Instrum. Meas. Technol. Conf. (I2MTC), May 2018, pp. 1-6.

[19] A. Foudazi, I. Mehdipour, K. M. Donnell, and K. H. Khayat, "Evaluation of steel fiber distribution in cement-based mortars using active microwave thermography," Mater. Struct., vol. 49, no. 12, pp. 5051-5065, Dec. 2016.

[20] A. Foudazi, C. A. Edwards, M. T. Ghasr, and K. M. Donnell, "Active Microwave Thermography for Defect Detection of CFRP-Strengthened Cement-Based Materials," IEEE Trans. Instrum. Meas., vol. 65, no. 11, pp. 2612-2620, Nov. 2016.

[21] A. Foudazi, M. T. Ghasr, and K. M. Donnell, "Characterization of corroded reinforced steel bars by active microwave thermography," IEEE Trans. Instrum. Meas., vol. 64, no. 9, pp. 2583-2585, Sep. 2015.

[22] A. Foudazi, M. T. Ghasr, and K. M. Donnell, "Application of active microwave thermography to inspection of carbon fiber reinforced composites," in Proc. IEEE AUTOTESTCON, Sep. 2014, pp. 318-322.

[23] A. Foudazi, K. M. Donnell, and M. T. Ghasr, "Application of active microwave thermography to delamination detection," in Proc. IEEE Int. Instrum. Meas. Technol. Conf. (I2MTC), May 2014, pp. 1567-1571.

[24] S. Keo, D. Defer, F. Breaban, and F. Brachelet, “Comparison between microwave infrared thermography and CO2 Laser infrared thermography in defect detection in applications with CFRP,” Mater. Sci. Appl., vol. 4, no. 10, pp. 600-605, 2013.

[25] U. Kaatze, “Complex permittivity of water as a function of frequency and temperature,” J. Chem. Eng. Data, vol. 34, no. 4, pp. 371–374, Oct. 1989.

[26] X. Maldague, “Introduction to NDT by active infrared thermography,” Mater. Eval., vol. 60, pp. 1060-1073, 2002.

[27] J. H. Lienhard IV, and J. H. Lienhard V, A Heat Transfer Textbook, 4th ed., Cambridge, Massachusetts, USA: Philogiston, 2017.

[28] K. Cole, A. Haji-Sheikh, J. Beck, and B. Litkouhi, Heat Conduction Using Green's Functions, New York, NY, USA:CRC Press, 2011.

[29] J. D. Jackson, Classical Electrodynamics, 3rd ed. New York: John Wiley & Sons, Inc, 1999.

[30] H. Hugli, J. Gonzalez, "Drop volume measurement by vision", SPIE Electronic Imaging Conference, vol. 3966, no. 11, pp. 60-66, 2000.

[31] W. M. Haynes, Ed., CRC Handbook of Chemistry and Physics. Boca Raton, FL, USA: CRC Press, 2016.

[32] E. M. Ortt et al, “A Device for Evaluating the Multiaxial Finite Strain Thermomechanical Behavior of Elastomers and Soft Tissues,” Journal of Applied Mechanics, vol. 67, pp. 465-471, Sep. 2000.

[33] B. Milovanović and I. Banjad Pečur, “Review of Active IR Thermography for Detection and Characterization of Defects in Reinforced Concrete,” Journal of Imaging, vol. 2, no. 2, pp. 11, 2016.

[34] R. Ross, “Inception and Propagation Mechanisms of Water Treeing,” IEEE Trans. Dielectr. Electr. Insul., vol. 5, pp. 660-680, 1998.

[35] M. Reid and P. Kilcullen, “Exploring Terahertz Waves for Submarine Cladding NDE: Tile Sealant Transmission Characterization, Instrument Field Housing Design/Prototype Option B: proof-of-concept concealed interface imaging,” University of Northern BC, Prince George, BC, Canada, Mar. 2017. [Online]. Available: https://cradpdf.drdc-rddc.gc.ca/PDFS/unc335/p809810_A1b.pdf.

[36] B. B. Lahiri, S. Bagavathiappan, P. R. Reshmi, J. Philip, T. Jayakumar, B. Raj, “Quantification of defects in composites and rubber materials using active thermography,” Infr. Phys. Technol, vol. 55, pp. 191-199, Mar. 2012.

[37] F. Xu et al, “Nondestructive Evaluation of Rubber Composites Using Terahertz Time Domain Spectroscopy,” in FIBRES & TEXTILES in Eastern Europe, 2018, iss. 1, no. 127, pp. 67-72.

[38] Z. Li, A. Haigh, C. Soutis, A. Gibson, and P. Wang, “A review of microwave testing of glass fibre-reinforced polymer composites,” Nondestruct. Test. Eva., vol. 34, no. 4, pp. 429-458, 2019.

[39] H. Deng, J. Ramos, and P. Yang, “Thermal Properties of a Glass Fiber Filled Epoxy (Sumitomo E264H),” The Rio Grande Symposium on Advanced Materials, 2015.

[40] HRH-10 Nomex Aramid Fiber / Phenolic Resin Product Data Sheet, HEXCEL®, 2017. [Online]. Available: https://www.hexcel.com/Resources/DataSheets/Honeycomb.

[41] A. Foudazi, I. Mehdipour, K. M. Donnell, and K. H. Khayat, “Evaluation of steel fiber distribution in cement-based mortars using active microwave thermography,” Mater. Struct., vol. 49, no. 12, pp. 5051-5065, Dec. 2016.

III. EFFICIENT HEALTH MONITORING OF RAM-COATED STRUCTURES BY ACTIVE MICROWAVE THERMOGRAPHY

ABSTRACT

In this paper, the application of active microwave thermography (AMT) is investigated as an efficient nondestructive (NDT) technique for health monitoring of structures coated with radio-frequency absorbing materials (RAM). The uniqueness of AMT for this particular application is the use of the microwave excitation which acts as a highly efficient thermal source due to the inherent absorptive electromagnetic properties of RAM-coated structures. In addition, the microwave induced heating takes place subsurface within the absorbing material of a RAM-coated structure, as opposed to the sole surface heating of conventional thermography. Specifically, this work focuses on detection of delamination, which is a common defect in carbon fiber reinforced polymer (CFRP) structures, via AMT. To this end, a comprehensive formulation and analysis method based on electromagnetic/thermal modeling is presented that enables estimating the output of an AMT inspection of a RAM-coated CFRP structure suffering from delamination. The effect the structure's constitutive properties, microwave excitation parameters, and the delamination size and depth on the defect detectability are investigated. In addition, several simulated and experimental results are provided that verify the accuracy of the proposed approach and show the high efficiency of AMT for detection of delamination in such structures.

1. INTRODUCTION

Radio-frequency (RF) absorbing materials (RAM) are widely used to reduce electromagnetic interference and scattering from reflective surfaces such as those utilized in aerospace and military applications. In particular for aerospace and military applications, structures of interest are often constructed of metals or several layers of carbon fiber reinforced polymer (CFRP) laminates. CFRP-based structures consist of carbon fibers embedded within a binding polymer matrix (usually an epoxy resin), effectively creating a CFRP laminate. These structures can sustain impact damage causing delamination in the CFRP that may not be readily visible through the RAM coating. Thus, it is important to nondestructively assess such structures for their structural health (i.e., defect detection).

Nondestructive testing (NDT) techniques for health monitoring of aerospace and military structures include microwave [1],[2], ultrasound [3], X-ray [4], and thermography [5]-[9]. Thermography in particular is a conventional NDT technique with a wide range of applications and many advantages including non-contact, fast inspection of relatively large areas, and easy-to-interpret results, amongst others. This technique can be applied in a passive or active manner, depending on the thermal excitation. In active thermography, heat (thermal energy) is induced into the structure under test by an active source, such as optical, electromagnetic, or acoustic [8]. More recently, active microwave thermography (AMT), a relatively new thermographic NDT approach that uses microwave radiation to create the thermal excitation, has been introduced into the NDT regime with promising results [10]-[20]. As it relates to structures with an RF/microwave absorbing surface (i.e., a RAM coating), when the structure is illuminated with microwave energy, a significant portion of this energy is absorbed and converted into thermal energy. Therefore, the RAM can serve as an efficient thermographic heat source to the underlying structure. The resulting surface thermal profile of the structure under inspection is measured with a thermal camera. In this way, subsurface defects present in the structure may affect the heat diffusion and present as indications in the resulting thermal image. AMT is an especially good candidate for inspection of such structures due to the inherent electromagnetic properties of the RAM itself. In other words, these materials are designed to reduce (through energy absorption) the amount of electromagnetic energy that is scattered (or reflected) from (subsurface) conductive materials. Thus, from an AMT perspective, the RAM, when under microwave illumination, absorbs the energy and subsequently undergoes a temperature increase; an essential component in thermographic techniques. In addition, unlike conventional thermography in which heat is generated mostly at the surface, the microwave heating takes place throughout the RAM volume (as well as its surface). In this way, the thermal source is located flush against the substructure rather than at the surface of the coating and hence the detection capability may be improved.

The utility of AMT for this application has been demonstrated in [14], where a thin RAM was placed on the surface of a CFRP laminate containing flat-bottom holes (FBH) as standardized defects. It has been shown that defects were easily detected when the RAM was present. This work extends this proof-of-concept work through a comprehensive electromagnetic/thermal formulation and analysis. Based on this and through simulated and experimental results, the potential for AMT to inspect for the presence of damage, specifically delamination, in RAM-coated CFRP structures, and the effect of parameters including the electromagnetic properties of the RAM, microwave excitation parameters (power, frequency, incidence angle, and polarization), and delamination size and depth are investigated.

2. MODELING AND FORMULATION

In AMT, the structure of interest is exposed to microwave radiation, often of medium power (on the order of tens of watts), which is directed by an antenna toward the structure under test. A portion of this energy is absorbed and subsequently converted into thermal energy and the rest is reflected back, as shown in Figure 1. The generated heat subsequently diffuses into the entire structure and causes a temperature distribution which is measured by a thermal (infrared) camera and subsequently processed in order to evaluate the structure for potential defects. In Figure 1, the structure (located in air) consists of a RAM layer with thickness, ℓ, and a substrate material with thickness, h, beneath that contains a defect. In order to obtain the heat source distribution within the RAM, the interaction of the incident electromagnetic wave and the structure is considered in the following subsection.

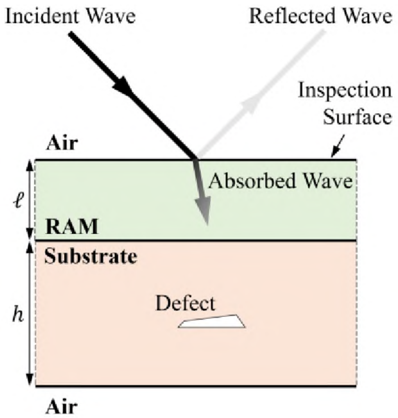

Figure 1. Schematic of a RAM-coated structure containing a defect under an AMT inspection

2.1. ELECTROMAGNETIC FORMULATION

The model of Figure 2 is used to formulate the heat source distribution induced by the microwave excitation. The formulation in this section is based on [21] and [22]. Figure 2 shows the incident, reflected, and penetrated electromagnetic fields over and inside the structure. To this end, the incident microwave energy is decomposed into perpendicular and parallel polarizations denoted by ⊥ and ||, respectively. Also, the superscripts *i* and *r* are used for the waves incident upon and reflected by the structure, and + and – represent the forward and reverse traveling waves inside the RAM. The RAM is taken as a dielectric with permittivity of ε and permeability of μ; both of which are complex and denoted as:

$$\begin{cases} \varepsilon = \varepsilon_0 \varepsilon_r = \varepsilon' - j\varepsilon'' \\ \mu = \mu_0 \mu_r = \mu' - j\mu'' \end{cases} \tag{1}$$

with ε_r and μ_r being the permittivity and permeability expressed relative to that of freespace, i.e., ε_0 and μ_0. The real parts of the complex permittivity and permeability, ε' and μ', determine the ability of the dielectric to store electromagnetic energy, while the imaginary parts, ε'' and μ'' (called electric and magnetic loss factors, respectively), identify the material's ability to absorb electric and magnetic energy. In other words, an electrically/magnetically lossy dielectric has a considerable electric/magnetic loss factor(s). In addition, for a nonzero electrical conductivity, σ, an additional loss mechanism, Joule heating, also takes place. In this case, σ can take effect by replacing ε'' with $\varepsilon'' + \sigma/\omega$ where ω is the microwave angular frequency. Lastly and since this work focuses on CFRP-based substrates, the substrate in this formulation is assumed to be a good conductor ($\sigma \approx \infty$), and therefore is reflective to incident microwave energy (as illustrated in Figure 2).

For non-scattering surfaces, incident and reflected microwave energy approaches and leaves a surface at the same angle relative to the surface normal direction. In air, this angle is denoted as θ in Figure 2. This angle is zero when the microwave antenna directs the radiation normal to the structure (which typically happens), however, can be nonzero for curved surfaces or corner inspections, or when the antenna is deployed off-normal due to space limitations or to allow a normal view for the thermal camera. The angle of refraction into the RAM is denoted as θ′, and from Snell's law, these two angles can be determined from the properties of the two mediums. In particular, the relationship is expressed as $ksin(\theta') = k_0 sin(\theta)$ where $k = \omega\sqrt{\varepsilon\mu}$ and $k_0 = \omega\sqrt{\varepsilon_0\mu_0}$ are the RAM and the freespace wavenumbers, respectively.

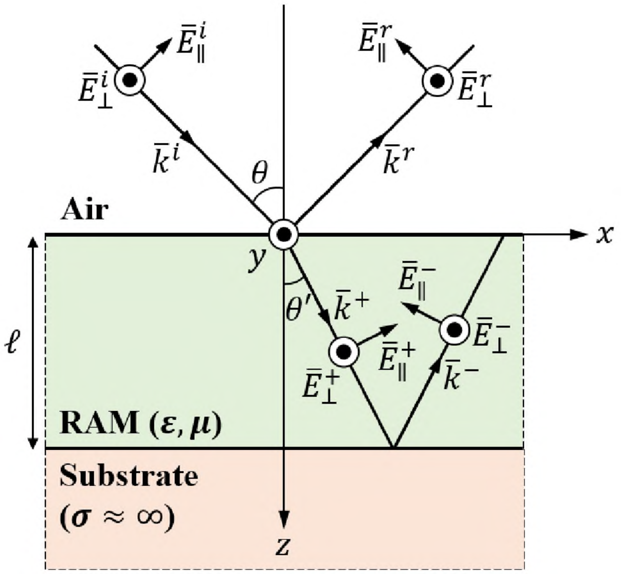

Figure 2. Interaction of electromagnetic fields with a RAM-coated conductive structure

The electric and magnetic fields inside the RAM can be determined by applying the boundary conditions at each medium interface. In particular, the continuity of tangential electric fields of the perpendicular and parallel polarizations at the air-RAM interface is:

$$\begin{cases} E_{\perp}^{i} + E_{\perp}^{r} = E_{\perp}^{+} + E_{\perp}^{-} \\ cos(\theta)\left(E_{\parallel}^{i} - E_{\parallel}^{r}\right) = cos(\theta')\left(E_{\parallel}^{+} - E_{\parallel}^{-}\right) \end{cases} \quad z = 0 \tag{2}$$

Also at this boundary, the tangential magnetic fields are continuous, and therefore:

$$\begin{cases} \dfrac{cos(\theta)}{\eta_0}\left(E_{\perp}^{i} - E_{\perp}^{r}\right) = \dfrac{cos(\theta')}{\eta}\left(E_{\perp}^{+} - E_{\perp}^{-}\right) \\ \dfrac{1}{\eta_0}\left(E_{\parallel}^{i} + E_{\parallel}^{r}\right) = \dfrac{1}{\eta}\left(E_{\parallel}^{+} + E_{\parallel}^{-}\right) \end{cases} \quad z = 0 \tag{3}$$

where $\eta = \sqrt{\mu/\varepsilon}$ and $\eta_0 = \sqrt{\mu_0/\varepsilon_0}$ are the intrinsic impedances of the RAM and freespace, respectively. Finally, at the interface of the RAM and the substrate, the tangential electric fields should be zero (as the substrate is a good conductor), then:

$$\begin{cases} E_{\perp}^{+} + E_{\perp}^{-} = 0 \\ E_{\parallel}^{+} - E_{\parallel}^{-} = 0 \end{cases} \quad z = \ell \tag{4}$$

Utilizing the boundary conditions of (2)-(4), the electric field components inside the RAM can be determined as:

$$E_{\perp}^{\pm} = \pm \frac{\eta cos(\theta) e^{\pm jk_z(\ell - z)}}{\eta_0 cos(\theta') cos(k_z \ell) + j\eta cos(\theta) sin(k_z \ell)} E_{\perp}^{i} \tag{5}$$

$$E_{\parallel}^{\pm} = \frac{\eta cos(\theta) e^{\pm jk_z(\ell - z)}}{\eta_0 cos(\theta) cos(k_z \ell) + j\eta cos(\theta') sin(k_z \ell)} E_{\parallel}^{i} \tag{6}$$

where $k_z = kcos(\theta')$. The absolute values of the electromagnetic fields in (5) and (6) can be found from:

$$E_{\perp}^{i} = \sqrt{2\eta_0 P_{\perp}^{i}} \ \ , \ \ E_{\parallel}^{i} = \sqrt{2\eta_0 P_{\parallel}^{i}} \tag{7}$$

In these equations, $P_{\perp}^{i}$ and $P_{\parallel}^{i}$ represent the power density of the perpendicular and parallel incident waves. Then, by having the components of the incident electric fields, the total electric and magnetic fields inside the RAM can be obtained from the model of Figure 2 as:

$$\begin{aligned} \bar{E} &= cos(\theta')\left(E_{\parallel}^{+} - E_{\parallel}^{-}\right)\hat{x} + (E_{\perp}^{+} + E_{\perp}^{-})\hat{y} \\ &\quad -sin(\theta')\left(E_{\parallel}^{+} + E_{\parallel}^{-}\right)\hat{z} \end{aligned} \tag{8}$$

$$\begin{aligned} \eta\bar{H} &= -cos(\theta')(E_{\perp}^{+} - E_{\perp}^{-})\hat{x} + \left(E_{\parallel}^{+} + E_{\parallel}^{-}\right)\hat{y} \\ &\quad +sin(\theta')(E_{\perp}^{+} + E_{\perp}^{-})\hat{z} \end{aligned} \tag{9}$$

Equations (8) and (9) can be used to determine the heat generated by the microwave excitation as:

$$Q = Q_e + Q_m = \pi f(\varepsilon''|E|^2 + \mu''|H|^2) \tag{10}$$

where Q_e and Q_m are the electric and magnetic heat densities, respectively (expressed in watts per cubic meter). The distribution of heat density, Q, inside the structure is used in the heat equation to obtain the temperature distribution inside and over the surface of the structure.

An active thermography test can be successful only if the excitation causes a significant temperature rise (relative to the measurable temperature limit), as the temperature variations are used to detect and evaluate defects. As the temperature rise is directly related to the induced heat, the total absorbed power (or equivalently induced heat) relative to the total incident power of the microwave excitation can be used to evaluate the efficiency of an AMT test. This ratio can be calculated as:

$$\mathcal{P} = \frac{P^a}{P^i} = \frac{(1 - |\Gamma_\perp^2|)P_\perp^i + \left(1 - \left|\Gamma_\parallel^2\right|\right)P_\parallel^i}{P_\perp^i + P_\parallel^i} cos(\theta) \tag{11}$$

where $\Gamma_\perp$ and $\Gamma_\parallel$ are the reflection coefficients of the perpendicular and parallel polarizations, respectively, and can be calculated from (2)-(6) as:

$$\Gamma_{\perp}=\frac{E_{\perp}^{r}}{E_{\perp}^{i}}=\frac{\eta cos(\theta)sin(k_z\ell)+j\eta_0 cos(\theta')cos(k_z\ell)}{\eta cos(\theta)sin(k_z\ell)-j\eta_0 cos(\theta')cos(k_z\ell)} \tag{12}$$

$$\Gamma_{\parallel}=-\frac{E_{\parallel}^{r}}{E_{\parallel}^{i}}=\frac{\eta cos(\theta')sin(k_z\ell)+j\eta_0 cos(\theta)cos(k_z\ell)}{\eta cos(\theta')sin(k_z\ell)-j\eta_0 cos(\theta)cos(k_z\ell)} \tag{13}$$

The normalized absorbed power, $\mathcal{P}$, in (11) is a function of the electromagnetic properties of the RAM, the layer thickness, and the parameters of the microwave excitation including frequency, incident angle, and polarization. This quantity will be used to study the effect of microwave excitation parameters on absorbed power.

2.2. THERMAL FORMULATION

To characterize defects using AMT, the correlation between a measured surface thermal profile and a potential defect must be established. To this end, the model of Figure 3 will be considered for the thermal model formulation. Here, the defect in question is assumed to be a delamination located between two CFRP layers in the structure, and is defined as a disk of diameter, D, located a depth, d, from the CFRP-RAM interface as shown in Figure 3. Thermally, the delamination is treated as a vacuum, meaning it is a void that has an infinite thermal resistance that fully obstructs the flow of heat normal to its surface. This property causes a higher temperature over the delamination because it blocks heat from flowing deeper into the CFRP. With thermal imaging, this hotspot will stand out relative to the adjacent surface area without any subsurface defects.

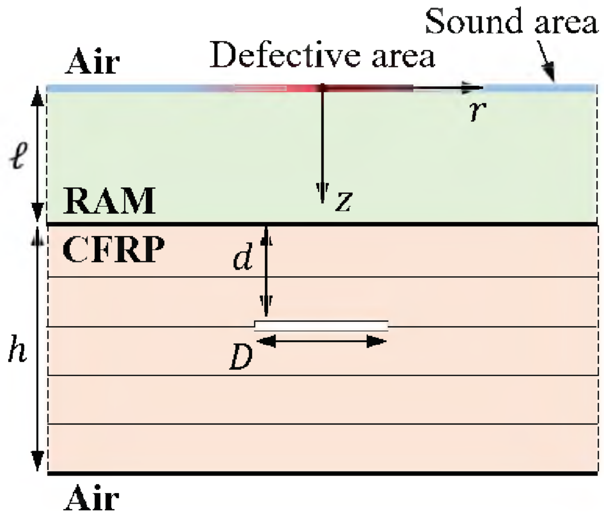

Figure 3. Geormetry of a RAM-coated CFRP structure containing a delamination

For calculation of the temperature distribution, the heat equation presented in [23]

$$\rho c \, {}^{\partial T}/_{\partial t} = \nabla \cdot (\boldsymbol{k} \cdot \nabla T) + Q \tag{14}$$

should be solved where ρ, c, and $\boldsymbol{k}$ denote the density, specific heat capacity, and thermal conductivity tensor, respectively. It should be noted that in this paper, the temperature variable, T, is the temperature increase from the initial (at $t = 0$) temperature and caused by microwave heating and does not reflect the initial temperature distribution inside the structure. For the experimental results to hold this assumption, the initial temperature values are subtracted from the measured temperature for all time. As the geometry of the defect in Figure 3 has a cylindrical symmetry, the heat equation of (14) can be written in cylindrical coordinates as:

$$\rho c\frac{\partial T}{\partial t}=\frac{1}{r}\frac{\partial}{\partial r}\left(rk_r\frac{\partial T}{\partial r}\right)+\frac{\partial}{\partial z}\left(k_z\frac{\partial T}{\partial z}\right)+Q \tag{15}$$

where the anisotropy of the CFRP (as the existence of carbon fibers along the in-plane directions causes a higher in-plane thermal conductivity than the transverse) is considered by assigning k_r and k_z for the in-plane and transverse components, respectively, of the thermal conductivity.

This equation should be solved numerically due to the complexity of the model. To this end, the space and time coordinates are discretized as $r = i\Delta r$, $z = j\Delta z$, and $t = k\Delta t$ where $i,j,k = 0,1,2,\ldots$ and Δr, Δz, and Δt are space and times steps. Using a forward-time centered-space (FCTS) scheme, finite difference approximations to each term in (15) can be written as [24]:

$$\rho c\frac{\partial T}{\partial t}\cong \rho(i,j)c(i,j)\frac{T^{k+1}(i,j)-T^{k}(i,j)}{\Delta t} \tag{16}$$

$$\begin{aligned}\frac{1}{r}\frac{\partial}{\partial r}\left(rk_r\frac{\partial T}{\partial r}\right)\cong{}&\frac{(i+1/2)k_r(i+1/2,j)}{i\Delta r}\frac{T^{k}(i+1,j)-T^{k}(i,j)}{\Delta r}-\\&\frac{(i-1/2)k_r(i-1/2,j)}{i\Delta r}\frac{T^{k}(i,j)-T^{k}(i-1,j)}{\Delta r}\end{aligned} \tag{17}$$

$$\begin{aligned}\frac{\partial}{\partial z}\left(k_z\frac{\partial T}{\partial z}\right)\cong{}&\frac{k_z(i,j+1/2)}{\Delta z}\frac{T^{k}(i,j+1)-T^{k}(i,j)}{\Delta z}-\\&\frac{k_z(i,j-1/2)}{\Delta z}\frac{T^{k}(i,j)-T^{k}(i,j-1)}{\Delta z}\end{aligned} \tag{18}$$

$$Q\cong Q^{k}(i,j) \tag{19}$$

Also, to ensure stability of the FTCS scheme, the following condition should be met:

$$\Delta t \leq min\left\{\frac{\rho c}{2k(1/\Delta r^2 + 1/\Delta z^2)}\right\} \tag{20}$$

In AMT, the microwave excitation is typically applied as a rectangular pulse consisting of a heating period, denoted by τ, in which the radiation is applied and a cooling period when the microwave excitation is removed and hence $Q = 0$ for $t > \tau$.

Obtaining the solution to equations (16)-(19) requires thermal boundary conditions to be applied. To simplify the problem while maintaining accuracy, adiabatic boundary conditions are assumed on all boundaries, including the top and bottom surfaces and normal to the delamination. Mathematically speaking, $\partial T/\partial n = 0$ where n denotes the normal to the boundaries.

Using this numerical technique is advantageous over commercial electromagnetic/thermal simulation software packages since it utilizes an analytical electromagnetic solution instead of a time-consuming full-wave numerical solution. Furthermore, the spatial two-dimensional heat transfer equation given in (14),has two spatial coordinates, r and z, rather than the typical three-dimensional simulation. Therefore, the simulations may run remarkably faster while providing accurate results. The simulation time becomes particularly important when a range of a particular parameter must be studied. In such a case, the model is repeatedly solved in order to find the relationship between thermal response and those parameters, and the overall solution time can become quite lengthy.

Finally, the thermal contrast (TC) is defined as the contrast between the temperature rise distributions caused by applying excitation centered over a defective area (T_D) versus a structurally sound area (T_S), or mathematically:

$$TC = T_D - T_S \tag{21}$$

A TC profile, according to this definition, has its maximum value near the center of delamination and reduces asymptotically from the center.

3. SIMULATIONS

To verify the proposed formulation and investigate the effect of different parameters on AMT outcomes, a number of simulations were conducted. This was accomplished through numerical evaluation of the above formulation in MATLAB and coupled electromagnetic/thermal models in CST Microwave Studio® and Multiphysics Studio®.

First, the effect of the RAM's ε and μ is considered. Generally, a RAM is categorized as either magnetic, or electric. Magnetic RAM includes magnetic particles, often ferrites, that interact with the magnetic field and their lossy behavior can be characterized by their complex permeability [25]. On the other hand, electric RAM contains electrically lossy fibers, often carbon fibers, thereby having a complex permittivity with a significant loss factor [25]. To study the effect of RAM type on heat generation, a magnetic RAM with $\varepsilon_r = 1$, $\mu_r = 5 - j10$ and an electric RAM with $\varepsilon_r = 5 - j10$, $\mu_r = 1$ were considered. A thickness of 2 mm was used for both types. Figure 4 shows the absorbed power density distribution along the depth of the two RAMs when they are exposed to a 50 W, 2.4 GHz normally incident wave. These results are obtained through the evaluation of analytical expressions (Ana) and CST simulations (CST), and as can be seen, significant agreement is observed.

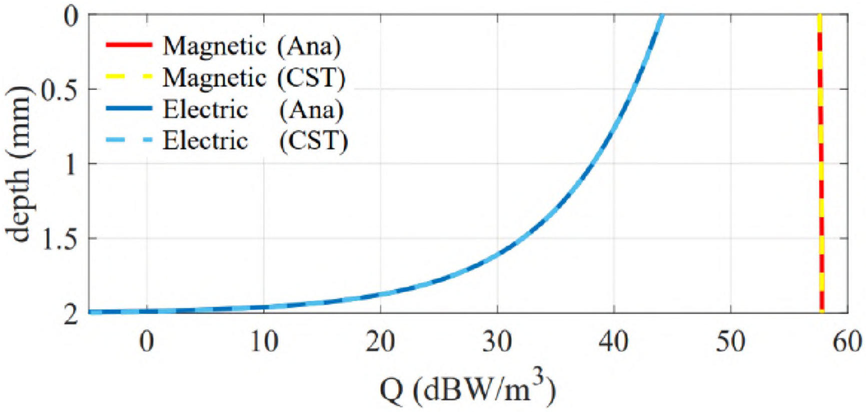

Figure 4. Absorbed power density (in dB) along the depth of the magnetic and electric RAMs obtained through analytical expressions and CST simulations

According to Figure 4, microwave radiation is more efficiently converted into heat with a magnetic RAM. The reason for this is that the conductive substrate eliminates the tangential electric field at the RAM-substrate boundary, leaving a very low absorbed power for any purely electric RAM. As seen in Figure 4, the loss density decreases along the depth of the electric RAM while it is uniform in the magnetic RAM. This behavior, however, is not necessarily true for other frequencies. To show the effect of frequency on the microwave absorption, the normalized absorbed power density, $\mathcal{P}$, is calculated from (11) and by CST and is shown versus frequency in Figure 5. At very low frequencies (<< 0.5

GHz), both magnetic and electric RAMs yield a small $\mathcal{P}$ since the RAM thickness is small relative to the wavelength (i.e., the RAM is electrically small) and so the incident wave reflects back from the substrate without effective interaction with the RAM (the wave doesn't "see" the RAM). At very high frequencies (> 35 GHz, in the present case), on the other hand, both types show the same behavior. In fact, in the high frequency limit ($f \rightarrow \infty$) with normal incidence ($\theta = 0$), (11) yields the same absorption for the two types. In this limit, the skin depth becomes infinitesimal and the incident wave is absorbed only at the surface of the RAM and does not interact with the substrate. It can be noted that as the energy is only absorbed by the surface of the structure in this limit, AMT is similar to conventional thermography with a continuous optical lamp (where heat is incident upon the surface only, because of the high frequency of the electromagnetic radiation generated by the optical/laser source). However, for lower frequencies, the absorption occurs through at least a portion of the volume of the RAM (and hence closer to potential defects in the substrate). As a result, AMT in such cases may present a better detection efficacy, especially when the RAM is considerably thick or has a low thermal conductivity (and hence acts as a thermal insulator concealing the substrate defect within).

As can also be seen in Figure 5, the maximum absorbed power density occurs for the magnetic and electric substrates at 2.2 and 13.8 GHz, respectively. To this end, (11) can be used to select the optimal operating frequency for an AMT inspection if the RAM properties are known or can be estimated. However, frequency selection may be limited in practice by the test equipment and government regulations.

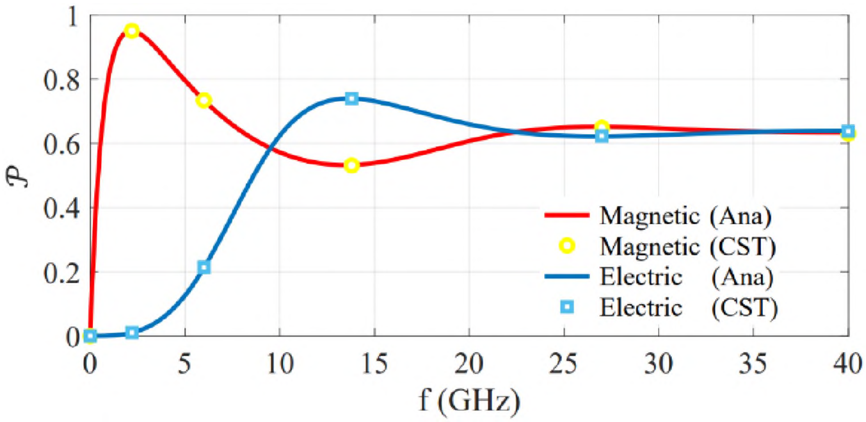

Figure 5. Normalized absorbed power density versus frequency for the two RAM types

Incident angle is also an important parameter that effects AMT outcome. As such, Figure 6(a) and (b) show $\mathcal{P}$ for magnetic and electric RAMs, respectively, as a function of incident angle at frequencies of 0.5, 2.2, and 5 GHz for perpendicular and parallel polarizations. According to Figure 6(a), $\mathcal{P}$ decreases with increasing incidence angle for all cases, but does so differently for the two polarizations. Specifically, at 0.5 GHz, a parallel polarization results in a higher absorption, while the two polarizations cause the same absorption at 2.2 GHz, and the absorption is lower for the parallel polarization than for the perpendicular polarization at 5.5 GHz. As a result, the selection of polarization is also important, and depends on the frequency for an optimized heat generation. In addition, the same quantity is represented for the electric RAM in Figure 6(b). In this case, the absorption is greater for the parallel polarization at all frequencies and angles. Also, the absorption increases with increasing incidence angle in some frequency ranges for the parallel polarization case. This is due to the fact that for the parallel (unlike perpendicular) polarization, the electric field component normal to the substrate boundary, which doesn't vanish at this boundary, is larger in magnitude for greater angles. Therefore, when illuminating a sample with an angle other than normal, use of the parallel polarization yields a better heat generation in an electric RAM. In addition, when the sample surface is not completely flat, such as a cylindrical surface, the polarization can be adjusted to obtain the least angle-dependent heating, while in the conventional (optical) thermography, the illumination (incident excitation intensity) suffers from the rapid degradation of cos(θ) [26].

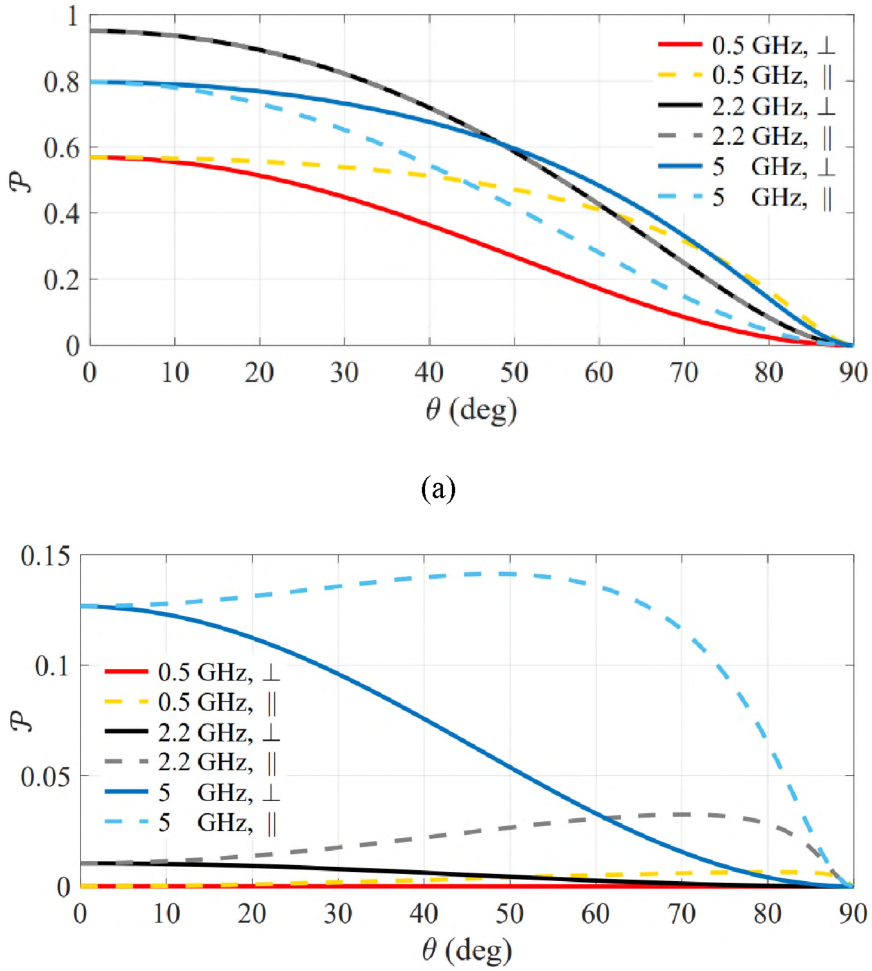

(a)

(b)

Figure 6. Normalized power density versus incidence angle for different frequencies and perpendicular and parallel polarizations for the (a) magnetic and (b) electric RAMs

Next, thermal simulation of AMT is considered. To this end, a RAM-coated CFRP structure with the RAM and CFRP thicknesses of 2 and 6 mm and the thermal properties given in Table 1, is considered. The thickness and thermal properties used for simulations were chosen to be consistent with the literature and the real materials considered in the next section. These results will be validated against the measurements presented in Section IV. In all following simulations, the microwave excitation is assumed to be 50 W of power at 2.4 GHz, and is applied for 180 sec. Further, the RAM is magnetic with $\mu_r = 2 - j0.2$.

Table 1. Thermal Properties of the RAM and CFRP [12],[26],[27]

Material	**k (W/m·K)**	**ρ (kg/m^3)**	**c (J/kg·K)**
RAM	0.85	3150	1300
CFRP	10 in-plane 1 transverse	1680	1200

The TC at the center of a delamination of a fixed depth, 0.8 mm, and varying diameters (2, 4, 6, 8, and 10 cm) is depicted in Figure 7(a). As expected, the TC has a higher value at any time for larger defects. However, the difference is small at the beginning of the heating period. This is because in the early instances of times, the TC at the center of the delamination is primarily affected by the middle area of the delamination as they are closer to each other, while it takes some time for the farther points of delamination (closer to its edges) to influence the TC at the center. Also, as can be seen in the figure, the TC does not grow linearly with the defect diameter. In fact, the difference between TC curves becomes less for larger defects, and as proven for the conventional thermography [28], TC asymptotically approaches its higher bound. Further, the rate of change of the TC versus time decays earlier for smaller diameters (see the 2 cm case, for example). This is because the lateral heat diffusion, which acts against the accumulation of thermal energy on the surface above of the defect, is stronger when defect has a smaller cross section. In other words, a larger cross section better maintains the accumulation of thermal energy, thereby resulting in a longer time of increasing temperature. This will be verified in the next section through measurement. Finally, it should be noted that the maximum of TC occurs with a delay from $t = 180$ sec (when the cooling period is removed). This is due to the nonzero depth of the RAM on top of the delamination which causes a delay for thermal energy to reach the surface.

Figure 7(b), shows the TC for a fixed diameter of 4 cm and depths of 0.8 - 4 mm. It can be seen in the figure that the depth of delamination has a significant effect on the TC. However, the shape of the curves remain consistent, and appear to be scaled versions of the same curve. As a rule of thumb, the TC is inversely proportional to the depth for an adiabatic (e.g., a void delamination) defect [28]. For the cases of Figure 7(b), the maximum of each curve is 0.51, 0.29, 0.17, 0.10, and 0.06, respectively, and rule of thumb appears to hold true. It is also important to note that the TC shown in Figure 7 is high relative to the typical thermal cameras' sensitivity, which is 0.03°C for the thermal camera used for measurements herein. This result demonstrates the efficacy of AMT for detection of delamination in RAM-coated CFRP structures. Lastly, these results will be validated by measurement in the next section.

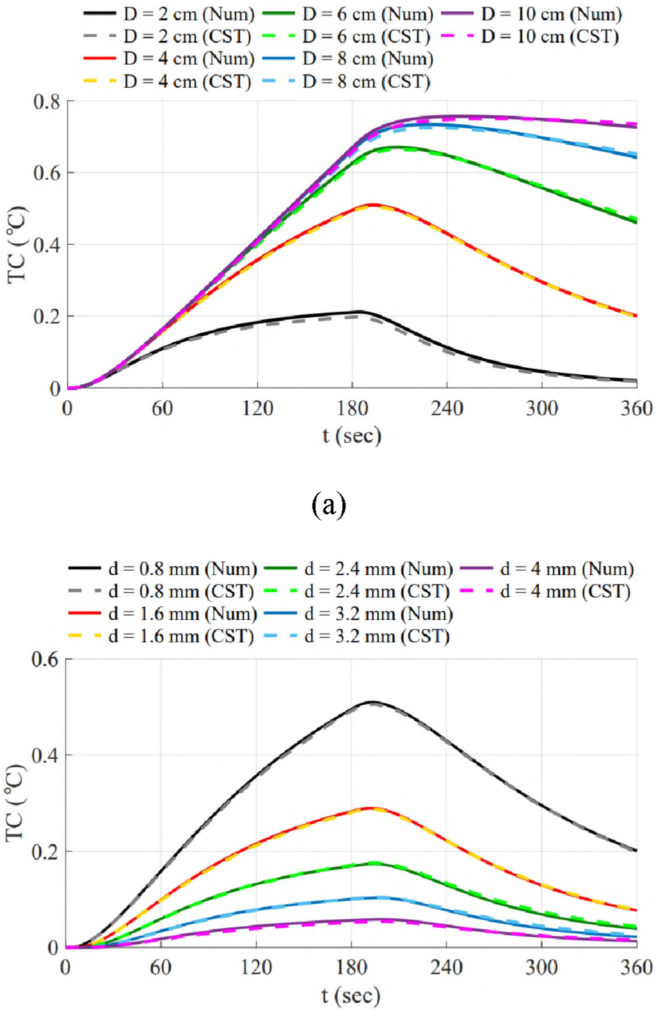

(a)

(b)

Figure 7. TC obtained through numerical analysis and CST simulations for different diameters (a) and depths (b)

4. MEASUREMENT RESULTS

A number of AMT measurements were conducted to show the applicability in detecting delamination in RAM-coated CFRP structures. To this end, the experimental setup shown in Figure 8 was used. The setup consists of a microwave source and 50 W amplifier operating at a frequency of 2.4 GHz for this work. This frequency is often used in AMT inspections because it is in the industrial, scientific, and medical (ISM) radio band. A thermal camera (FLIR T430sc) is used to measure the surface thermal profiles. The thermal camera, microwave source, and amplifier are controlled by a data acquisition (DAQ) and control unit. A horn antenna with aperture size of 23 × 17 cm^2 is used to direct the microwave radiation on the inspection surface. The antenna is placed at the lift-off distance from the structure in order to provide a sufficient microwave incident power and thermal camera field-of-view. For this work, the lift-off distance is 40 cm for all tests. In order to avoid thermal energy losses from the bottom of the structure (equivalent to the adiabatic boundary condition assumed in formulation and simulations), the structure was placed on polystyrene foam.

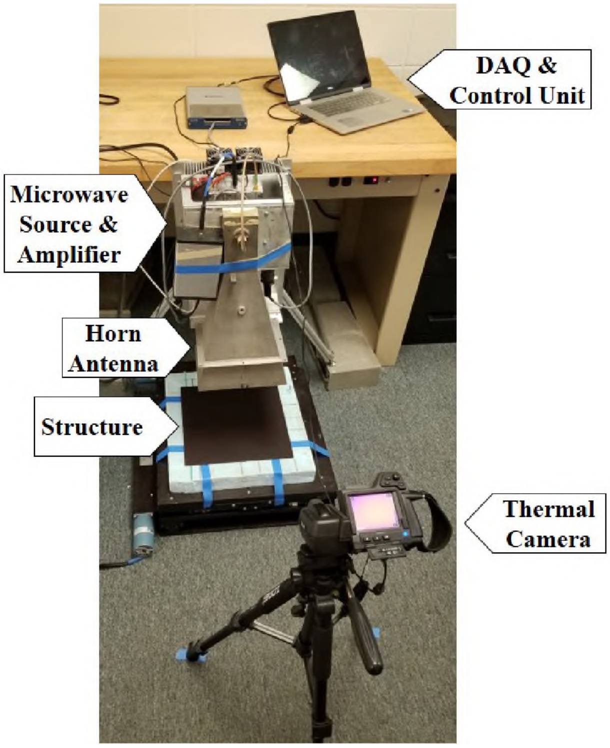

Figure 8. The experimental setup for AMT measurements

Two samples were constructed by stacking up a layer of RAM and seven layers of CFRP laminates, as shown in Figure 9(a). These layers were packed tightly to minimize formation of an air gap between the layers. Figure 9(b) shows the RAM used in this work; a Cuming Microwave C-RAM FF-2 magnetic-type absorber with a thickness of 2 mm. This absorber is a ferrite filled, silicone rubber sheet which has a high magnetic loss at microwave frequencies, and its density and thermal conductivity are 3150 kg/m^3 and 0.85 W/m·K, respectively [29]. Each substrate CFRP laminate is 0.8 mm thick, and the total thickness of the CFRP substrate is 6 mm. The density of each layer is measured 1680 kg/m^3. A delamination was introduced by machining a hole at the center of one of the CFRP layers, as shown in Figure 9(c). The measurements were done with three delaminations with D = 4 cm / d = 0.8 mm, D = 2 cm / d = 0.8 mm, and D = 4 cm / d = 1.6 mm, which will be called Case 1, Case 2, and Case 3, respectively. The heating and cooling times are 180 sec each for all measurements.

(a) (b) (c)

Figure 9. The RAM-coated CFRP structure: (a) stack-up, (b) top surface, and (c) a machined hole serving a as a delamination

Figure 10 shows the temperature rise (with respect to the initial temperature) distribution in AMT tests at t = 180 sec and measured for the three cases along with the case with no delamination. More specifically, the temperature rise is depicted as a function of radial distance from the center of the delamination. The measurement without any delamination provides a visual contrast as to how a delamination introduces local hotspots during an AMT inspection. As seen in the figure, with the presence of a delamination, the temperature peaks at the center of the delamination and asymptotically approaches that of the case without a delamination. A comparison between the curves of Figure 10 shows that, as expected, a larger diameter and/or smaller depth yields a higher temperature rise on top of the delamination. In addition, as seen in the figure, for the deeper delamination case (d = 1.6 mm), T is flatter at the center, with respect to the d = 0.8 mm cases. In fact, the thermal energy diffuses with less constraint over a deeper defect, causing a flatter temperature profile. As a result, the thermal image over a deeper defect is fader and less representing the cross-sectional extension of the beneath the surface. This will be further shown in the thermal images (Figure 12).

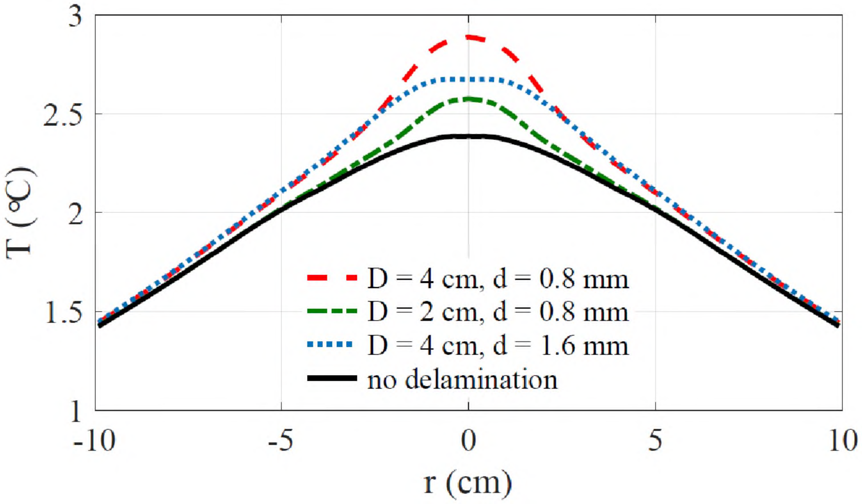

Figure 10. Temperature increase after 180 sec of microwave excitation versus radial distance from the delamination for different delamination diamater and depth and the case of no delamination

To better observe the temperature distribution shaped by the radiation pattern of the horn antenna and the existence of a delamination, T_D, T_S, and TC profiles, as defined in (21), are illustrated at t = 180 sec in Figure 11. The dashed circle shows the physical cross-section of the delamination inside the structure. As is apparent in the TC profile, the presence of the delamination maximally affects the temperature within the cross-sectional boundaries of the delamination. However, due to the heat diffusion, it also affects the temperature beyond this boundary. Also, it can be noted from the T_S profile that the antenna's heating pattern is focused in an area of approximately 20 × 20 cm^2. This indicates the maximum efficient inspection area in a single test. In the case a larger area is required for inspection, an antenna (or an array of antennas) with a wider radiation pattern should be employed, or a raster scanning can be performed.

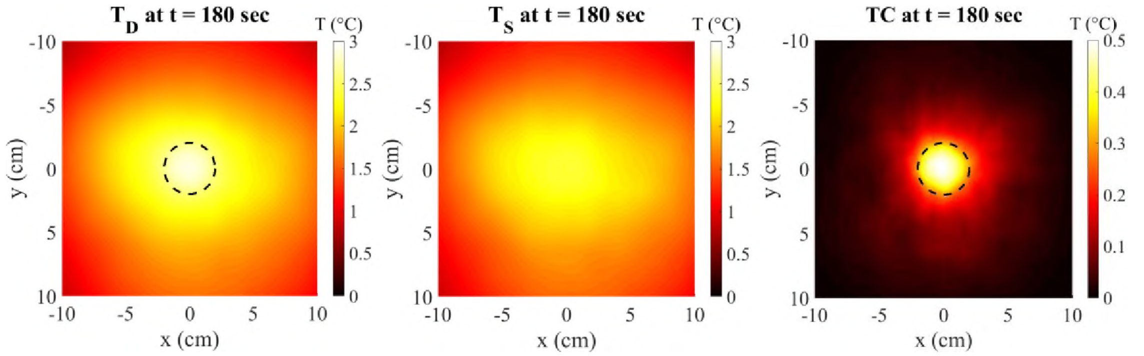

Figure 11. T_D, T_S, and TC profiles at t = 180 sec for Case 1

An additional illustration of the spatial and temporal variations of an AMT measurement is shown in Figure 12, where TC's for the three cases at times of 60, 120, 180, and 300 seconds are shown (heating time of 180 sec). As seen in the figure, the defects are observable after 60 sec of microwave heating, and they become highly apparent at

180 sec. More specifically, the TC profiles show a hot area on the structure surface in the area above the defect cross section as outlined by the dotted circles. For the deepest delamination (d = 1.6 mm), the temperature spreads more to the outside of the delamination. This is because the thermal energy spreads more extensively before reaching the surface for a deeper defect. As a result, the spatial temperature distribution is better confined to the corresponding physical distribution when the defect is closer to the surface and therefore is a better indication of the cross-sectional extension of the defect. Also, it can be noted that unlike the D = 4 cm cases, the D = 2 cm case has an insignificant change from *t* = 120 sec to 180 sec. This is consistent with simulation results presented in Section III, Figure 7(a), where the temperature rise and rate of change is less for a smaller defect.

To verify the proposed mathematical modeling and analysis presented above, the TC at the center of the delamination is demonstrated versus time in Figure 13 and compared to those calculated numerically and given in Figure 7. It can be seen that there is excellent agreement between the experimental and mathematical results that validates the electromagnetic/thermal model and formulation. More specifically, the TC values reach the 0.03 °C threshold (shown with the dashed line in the figure) at *t* = 23, 24, and 30 sec for Cases 1, 2 and 3, respectively. These heating times can be theoretically considered the minimum required heating times for a successful defect detection. Further, after one minute of microwave heating, all three cases yield a TC of >> 0.03 °C, making the defects readily observed as was demonstrated in Figure 12.

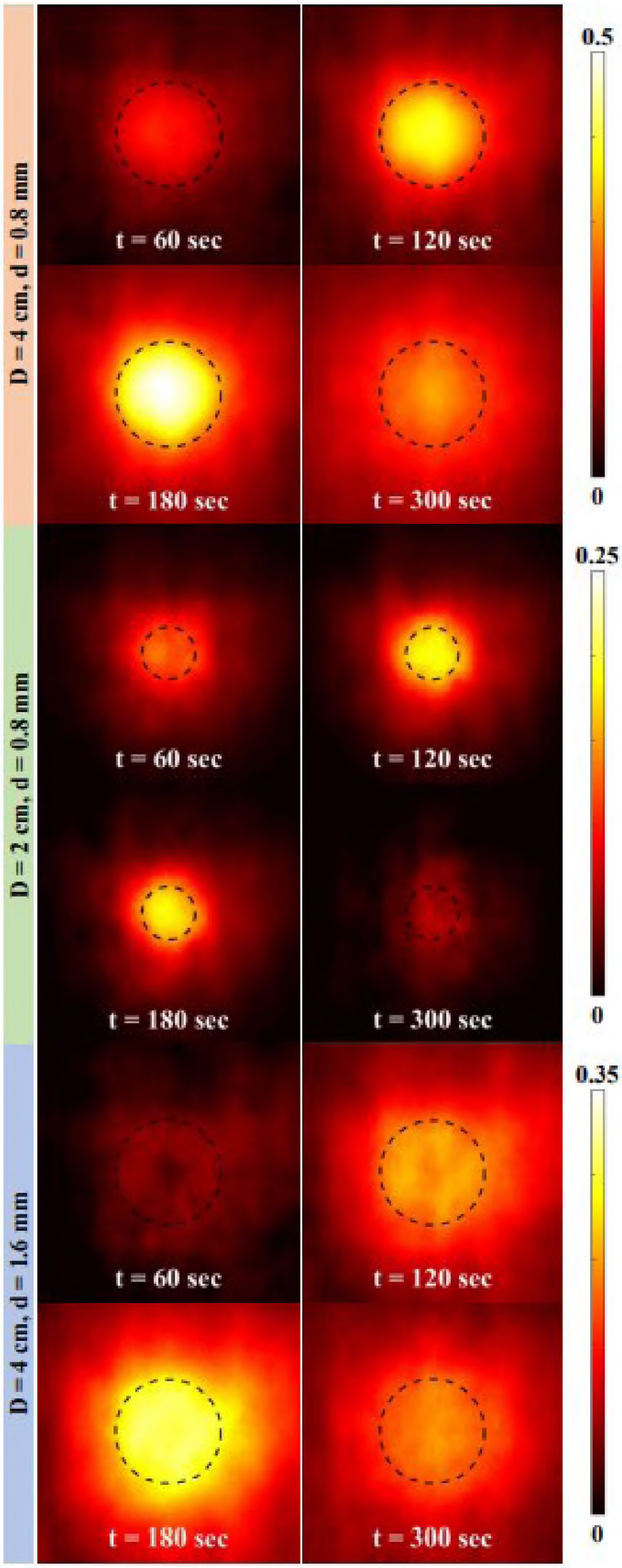

Figure 12. TC profiles (unit: °C) at different times for delmainations of given diameters and depths

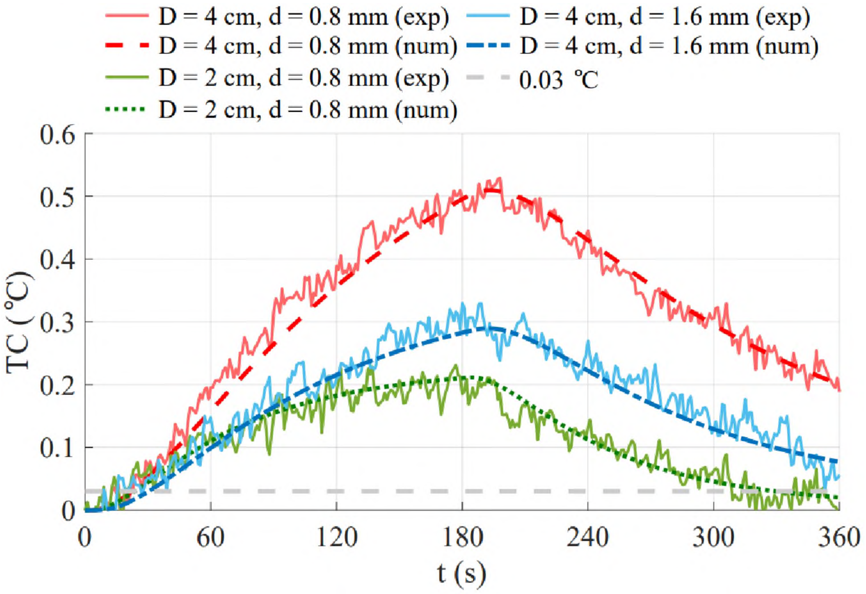

Figure 13. TC over time obtained experimentally and numerically

5. CONCLUSION

Active microwave thermography (AMT) was considered as a nondestructive testing tool for inspection of RAM-coated electromagnetically reflective (such as CFRP) structures that are extensively used in military and aerospace applications. Detection of a delamination with different diameters and depths was considered. A mathematical model was proposed that relates the thermal contrast (TC) to the defect, microwave excitation, and the structure properties. The effect of delamination size and depth was studied through simulation and measurement results. AMT measurements support the proposed modeling and formulation as well as show the applicability and efficacy of this approach for detection of a delamination in RAM-coated CFRP structures. More specifically, it was shown that delaminations with a diameter as small as 1 cm concealed under a 2-mm thick layer of RAM can be reliably detected by applying 1 minute of microwave excitation. Overall, due to the interaction of microwave energy and RAM coatings (i.e. inherent absorbing properties of RAM), this new proposed technique may be advantageous as compared to other thermographic techniques for inspection of RAM-coated structures.

REFERENCES

[1] R. Zoughi, Microwave non-destructive testing and evaluation principles, vol. 4, Dordrecht, The Netherlands: Kluwer, 2000.

[2] A. Mirala, and R. Sarraf Shirazi, "Detection of surface cracks in metals using time-domain microwave non-destructive testing technique," IET Microw. Antennas Propag., vol. 11, Iss. 4, pp. 564-569, Mar. 2017.

[3] M. Ricci, L. Senni, and P. Burrascano, "Exploiting pseudorandom sequences to enhance noise immunity for air-coupled ultrasonic nondestructive testing," IEEE Trans. Instrum. Meas., vol. 61, no. 11, pp. 2905-2915, Nov. 2012.

[4] S. C. de Wolski, J. E. Bolander, and E. N. Landis, "An in-situ X-ray microtomography study of split cylinder fracture in cement-based materials," Experimental Mechanics, vol. 54, no. 7, pp. 1227-1235, May 2014.

[5] K. Srinivas, A. O. Siddiqui, and J. Lahiri, "Thermographic inspection of composite materials," in Proc. Nat. Seminar Non-Destruct. Eval., vol. 12, pp. 7–9, 2006.

[6] C. Ibarra-Castanedo, and X. Maldague, "Infrared thermography," in Handbook of Technical Diagnostics, Springer-Verlag Berlin Heidelberg, 2013, pp. 175-220.

[7] A. Poudel, K. R. Mitchell, T. P. Chu, S. Neidigk, and C. Jacques, "Non-destructive evaluation of composite repairs by using infrared thermography," Journal of Composite Materials, vol. 50, no. 3, pp. 351-363, Feb. 2016.

[8] R. Yang, and Y He, "Optically and Non-optically Excited Thermography for Composites: A Review," Infrared Physics & Technology, vol. 75, pp. 26-50, Mar. 2016.

[9] H. Zhang, R. Yang, Y. He, A. Foudazi, L. Cheng, and G. Tian, "A Review of Microwave Thermography Nondestructive Testing and Evaluation," Sensors, vol. 17, no. 5, 2017.

[10] A Mirala, A. Foudazi, M. T. Ghasr, and K. M. Donnell, "Detection of Flat-Bottom Holes in Conductive Composites Using Active Microwave Thermography," ASME J Nondestrcutve Evaluation, vol. 1, Iss. 4, pp. 041005-1-041005-7, Nov. 2018.

[11] A. Foudazi, A. Mirala, M. T. Ghasr, and K. M. Donnell, "Active Microwave Thermography for Nondestructive Evaluation of Surface Cracks in Metal Structures," IEEE Trans. Instrum. Meas., vol. 68, no. 2, pp. 576-585, Feb. 2019.

[12] A Mirala and K. M. Donnell, "Active Microwave Thermographic Measurement of In-Plane Thermal Diffusivity," to be publisehd in Proc. IEEE Int. Instrum. Meas. Technol. Conf. (I2MTC), May 2020.

[13] A Mirala, X. Zou, M. T. Ghasr, L. Sneed, and K. M. Donnell, "Active Microwave Thermography: A Real-Time Monitoring Tool for CFRP-Concrete Bond Testing," in Proc. IEEE Int. Instrum. Meas. Technol. Conf. (I2MTC), May 2019, pp. 1-6.

[14] A Mirala, M. T. Ghasr, and K. M. Donnell, "Nondestructive assessment of microwave absorbing structures via active microwave thermography," in Proc. IEEE Int. Instrum. Meas. Technol. Conf. (I2MTC), May 2018, pp. 1-6.

[15] A. Foudazi, I. Mehdipour, K. M. Donnell, and K. H. Khayat, "Evaluation of steel fiber distribution in cement-based mortars using active microwave thermography," Mater. Struct., vol. 49, no. 12, pp. 5051-5065, Dec. 2016.

[16] A. Foudazi, C. A. Edwards, M. T. Ghasr, and K. M. Donnell, "Active Microwave Thermography for Defect Detection of CFRP-Strengthened Cement-Based Materials," IEEE Trans. Instrum. Meas., vol. 65, no. 11, pp. 2612-2620, Nov. 2016.

[17] A. Foudazi, M. T. Ghasr, and K. M. Donnell, "Characterization of corroded reinforced steel bars by active microwave thermography," IEEE Trans. Instrum. Meas., vol. 64, no. 9, pp. 2583-2585, Sep. 2015.

[18] A. Foudazi, M. T. Ghasr, and K. M. Donnell, "Application of active microwave thermography to inspection of carbon fiber reinforced composites," in Proc. IEEE AUTOTESTCON, Sep. 2014, pp. 318-322.

[19] A. Foudazi, K. M. Donnell, and M. T. Ghasr, "Application of active microwave thermography to delamination detection," in Proc. IEEE Int. Instrum. Meas. Technol. Conf. (I2MTC), May 2014, pp. 1567-1571.

[20] S. Keo, D. Defer, F. Breaban, and F. Brachelet, "Comparison between microwave infrared thermography and CO2 Laser infrared thermography in defect detection in applications with CFRP," Mater. Sci. Appl., vol. 4, no. 10, pp. 600-605, 2013.

[21] D. M. Pozar, Microwave Engineering, 4th ed. Hoboken, NJ, USA: Wiley, 2012.

[22] C. A. Balanis, Advanced Engineering Electromagnetics, Hoboken, NJ, USA:Wiley, 2012.

[23] J. H. Lienhard IV, and J. H. Lienhard V, A Heat Transfer Textbook, 4th ed., Cambridge, Massachusetts, USA: Philogiston, 2017.

[24] R. H. Pletcher, J. C. Tannehill, and D. A. Anderson, Computational Fluid Mechanics and Heat Transfer, 3rd ed., Boca Raton, FL, USA: CRC Press, 2012.

[25] G. Shen, M. Xu, and Z. Xu, “Double-layer microwave absorber based onferrite and short carbon fiber composites,” Materials Chemistry and Physics, vol. 105, pp. 268-272, 2007.

[26] G. Mayr, B. Dietermayr, G. Hendorfer, and J. Sekelja, “Characterization of Defects in Curved CFRP Samples using Pulsed Thermography and 3D Finite Element Simulation,” in Proc. 9th International Conference on Quantitative InfraRed Thermography, July 2008, Krakow, Poland.

[27] T. Tian and K. D. Cole, ”Anisotropic thermal conductivity measurement of carbon-fiber/epoxy composite materials,” International Journal of Heat and Mass Transfer, vol. 55, Iss. 23–24, pp. 6530-6537, 2012.

[28] M. F. Beemer, and S. M. Shepard, “Aspect ratio considerations for flat bottom hole defects in active thermography,” Quantitative InfraRed Thermography Journal, 2017.

[29] Cuming Microwave, C-RAM FF-2 Technical Bulletin, [Online]. Available: https://www.cumingmicrowave.com/pdf/310-Rubber%20Sheets/310-7%20C-RAM%20FF-2.pdf.

SECTION

2. CONCLUSIONS AND FUTURE WORK

2.1. CONCLUSIONS

Active microwave thermography (AMT) has a wide range of applications in aerospace and infrastructure industries. The overarching objective of this work is to advance AMT as a reliable nondestructive testing (NDT) tool for detection of several types of defects (void, water ingress, delamination, etc.) in various structures. In this dissertation, three special applications of AMT were considered as follows.

In PAPER I, AMT was considered for detection of void-type defects, commonly standardized as flat-bottom holes (FBH), in conductive composites, specifically carbon fiber reinforced polymer (CFRP). More specifically, the effect of FBH radius and depth (or combined as the radius-to-depth ratio) on the detection likelihood was studied through simulation and measurement. By considering the thermal contrast (i.e., difference between the temperature increase of a defective area and that of a sound/healthy area), it was shown that detection likelihood can be improved by increasing the operating frequency or power level of the microwave excitation. Furthermore, AMT measurements were conducted for a number of FBHs machined in a multidirectional CFRP sheet, and the signal-to-noise ratio (SNR) in thermal images over time was monitored, which showed that a high level of defect information relative to background noise (>20 dB) is achievable after approximately 60 s of microwave excitation.

In PAPER II, AMT was used for detection and evaluation of water ingress in different materials, in particular rubber. Simulation and experimental results indicate that AMT has a strong potential to detect and locate small volumes of water ingress after a few minutes of microwave excitation. Specifically, 0.5 mL of water was clearly detected (experimentally) after 120 seconds of microwave excitation within a rubber sample. More importantly, the depth of water was estimated using experimental data and a mathematical formulation, with an average quantification error of ~5%. This was accomplished by relating the temporal behavior of the thermal response of the structure containing water ingress to 300 seconds of constant microwave excitation. In addition, the relationship between the detectability of water and test parameters including the microwave excitation frequency and power, water volume and depth, structure constitutive properties, and heating time was established.

PAPER III was dedicated to a comprehensive study of AMT for inspection of electromagnetically reflective (such as CFRP) structures coated with radio-frequency absorbing materials (RAM), that are extensively used in military and aerospace applications. Due to the interaction of microwaves with RAMs, the new proposed technique may be uniquely advantageous to other thermographic techniques for inspection of RAM-coated structures. As such, detection of delaminations with different diameters and depths within a substrate (specifically, CFRP laminates) that is covered by RAM was considered. To this end, a mathematical model was developed that related the thermal contrast to the delamination, microwave excitation, and the structure properties. It was shown that AMT measurements support the proposed modeling and formulation as well as show the applicability and efficacy of this approach. More specifically, it was shown that delaminations with a diameter as small as 1 cm concealed under a 2-mm thick layer of RAM can be reliably detected by applying 1 minute of microwave excitation.

2.2. FUTURE WORK

As has been shown, AMT has shown promise in various applications and is has been advanced both theoretically and practically. To further advance the method, future work is proposed as follows:

1- The applicability and potential of AMT for inspection of other structures such as honeycomb structures and glass fiber composites can be investigated. In particular, AMT may be a good candidate for evaluation of water ingress or moisture content in glass fiber reinforced polymers (GFRP), since GFRP has a very low electromagnetic loss, and microwave energy can readily penetrate into its depth and interact with water. This enables AMT to detect and evaluate water in deeper parts of a GFRP structure. This research can be very important since water absorption by GFRP structures degrades their mechanical performance [25]. Similar to this, estimation of moisture content of cement-based materials can be considered as another potential application for AMT.

2- The work of PAPER II can be extended to include inspection of the RAM itself (related to RAM-coated structures). More specifically, defects within the RAM including non-uniform thickness, existence of voids within the RAM, debonding between the RAM and substrate, etc. may be detected and/or evaluated via AMT.

3- Advanced theoretical and experimental investigation can be carried out to show the applicability of image processing methods to evaluate the cross-sectional extension of defects. These methods may be based on the gradient of the temperature profiles.

Preliminary results show that applying simple gradient or more advanced filters such as Sobel and Canny have a good potential for this application.

4- A complex microwave phased array radiating subsystem may be developed to provide an adjustable heating pattern; in particular to yield uniform heating. Specifically, a double-element phased array is already designed and tested that has an improved uniform heating pattern along one direction. This technique can be extended to two dimensions.

BIBLIOGRAPHY

1. R. Zoughi, Microwave non-destructive testing and evaluation principles, vol. 4, Dordrecht, The Netherlands: Kluwer, 2000.

2. A. Ebrahimkhanlou, A. Farhidzadeh, and S. Salamone, "Multifractal analysis of crack patterns in reinforced concrete shear walls," Struct. Health Monitor., vol. 15, no. 1, pp. 81–92, 2016.

3. A. Mirala, and R. Sarraf Shirazi, "Detection of surface cracks in metals using time-domain microwave non-destructive testing technique," IET Microw. Antennas Propag., vol. 11, Iss. 4, pp. 564-569, Mar. 2017.

4. M. Ricci, L. Senni, and P. Burrascano, "Exploiting pseudorandom sequences to enhance noise immunity for air-coupled ultrasonic nondestructive testing," IEEE Trans. Instrum. Meas., vol. 61, no. 11, pp. 2905–2915, Nov. 2012.

5. S. C. de Wolski, J. E. Bolander, and E. N. Landis, "An in-situ X-ray microtomography study of split cylinder fracture in cement-based materials," Experim. Mech., vol. 54, no. 7, pp. 1227–1235, Sep. 2014.

6. R. Yang and Y. He, "Optically and non-optically excited thermography for composites: A review," Infr. Phys. Technol., vol. 75, pp. 26–50, Mar. 2016.

7. C. Ibarra-Castanedo and X. P. V. Maldague, "Infrared thermography," in Handbook of Technical Diagnostics. Berlin, Germany: Springer, 2013, pp. 175–220.

8. K. Srinivas, A. O. Siddiqui, and J. Lahiri, "Thermographic inspection of composite materials," in Proc. Nat. Seminar Non-Destruct. Eval., vol. 12. 2006, pp. 7–9.

9. J. G. Thompson and C. T. Uyehara, "Ultrasonic thermography inspection method and apparatus," U.S. Patent 7 075 084, Jul. 11, 2006.

10. J. Saniie, M. Luukkala, A. Lehto, and R. Rajala, "Thermal wave imaging through radio frequency induction heating," Electron. Lett., vol. 18, no. 15, pp. 651–653, Jul. 1982.

11. H. Zhang, R. Yang, Y. He, A. Foudazi, L. Cheng, and G. Tian, "A Review of Microwave Thermography Nondestructive Testing and Evaluation," Sensors, vol. 17, no. 5, 2017.

12. A Mirala, A. Foudazi, M. T. Ghasr, and K. M. Donnell, “Detection of Flat-Bottom Holes in Conductive Composites Using Active Microwave Thermography,” ASME J Nondestrcutve Evaluation, vol. 1, Iss. 4, pp. 041005-1-041005-7, Nov. 2018.

13. A. Foudazi, M. T. Ghasr, and K. M. Donnell, “Application of active microwave thermography to inspection of carbon fiber reinforced composites,” in Proc. IEEE AUTOTESTCON, Sep. 2014, pp. 318-322.

14. A Mirala, M. T. Ghasr, and K. M. Donnell, “Nondestructive assessment of microwave absorbing structures via active microwave thermography,” in Proc. IEEE Int. Instrum. Meas. Technol. Conf. (I2MTC), May 2018. pp. 1-6.

15. A. Foudazi, A. Mirala, M. T. Ghasr, and K. M. Donnell, “Active Microwave Thermography for Nondestructive Evaluation of Surface Cracks in Metal Structures,” in IEEE Trans. Instrum. Meas., Jun. 2018.

16. A. Foudazi, M. T. Ghasr, and K. M. Donnell, “Characterization of corroded reinforced steel bars by active microwave thermography,” IEEE Trans. Instrum. Meas., vol. 64, no. 9, pp. 2583-2585, Sep. 2015.

17. A. Foudazi, I. Mehdipour, K. M. Donnell, and K. H. Khayat, “Evaluation of steel fiber distribution in cement-based mortars using active microwave thermography,” Mater. Struct., vol. 49, no. 12, pp. 5051-5065, Dec. 2016.

18. A. Foudazi, C. A. Edwards, M. T. Ghasr, and K. M. Donnell, “Active Microwave Thermography for Defect Detection of CFRP-Strengthened Cement-Based Materials,” IEEE Trans. Instrum. Meas., vol. 65, no. 11, pp. 2612-2620, Nov. 2016.

19. A. Foudazi, K. M. Donnell, and M. T. Ghasr, “Application of active microwave thermography to delamination detection,” in Proc. IEEE Int. Instrum. Meas. Technol. Conf. (I2MTC), May 2014, pp. 1567-1571.

20. D. Balageas and P. Levesque, “Mines detection using the EMIR method,” in Proc. QIRT, 2002, pp. 71–78.

21. D. M. Pozar, Microwave Engineering, 4th ed. Hoboken, NJ, USA: Wiley, 2012.

22. C. A. Balanis, Advanced Engineering Electromagnetics, Hoboken, NJ, USA:Wiley, 2012.

23. X. Maldague, “Introduction to NDT by active infrared thermography,” Mater. Eval., vol. 60, pp. 1060-1073, 2002.

24. K. Cole, A. Haji-Sheikh, J. Beck, and B. Litkouhi, Heat Conduction Using Green’s Functions, New York, NY, USA:CRC Press, 2011.

25. L. Rocha, “Combined experimental/numerical investigation of directional moisture diffusion in glass/epoxy composites,” Composites Science and Technology, vol. 151, pp. 16-24, Oct. 2017.

VITA

Ali Mirala received his B.Sc. degree in Electrical Engineering from Iran University of Science and Technology, Tehran, Iran in 2011 and M.Sc. degree from Amirkabir University of Technology (Tehran Polytechnic), Tehran, Iran, in 2014. He joined the Microwave Sensing (μSense) Laboratory at the Missouri University of Science and Technology (Missouri S&T) in Spring 2017 as a Ph.D. student. In May 2020, he received the Missouri S&T Dean's Ph.D. Scholar Award for his Ph.D. work. Ali received his Ph.D. in Electrical Engineering from Missouri University of Science and Technology in August 2020. His research interests included theoretical electromagnetics, microwave non-destructive testing (NDT) technique, multi-physical modeling and numerical analysis, and electromagnetic compatibility (EMC).